ADDITIVE DESIGN AND MANUFACTURING OF AIR-COOLED HEAT EXCHANGERS

by

Jake Boxleitner

A thesis submitted in partial fulfillment of

the requirements for the degree of:

Master of Science

(Mechanical Engineering)

at the

UNIVERSITY OF WISCONSIN - MADISON

2018

Approved by:

Professor Gregory F. Nellis Date

Emeritus Professor Sanford A. Klein Date

Professor Xiaoping Qian Date

Abstract

Air-cooled heat exchangers are an integral component in energy systems because many must ultimately reject or in some cases accept heat from atmosphere. The limiting factor for an air-cooled heat exchanger is the airside convection resistance due to low heat transfer coefficients related to the fluid's low density and low conductivity. Because of this, air-cooled heat exchangers are a prime candidate to be redesigned using the extra degrees of freedom enabled with additive manufacturing to construct an airside geometry capable of out-performing existing technologies.

This work aims to couple deposition based additive manufacturing constraints with heat transfer and fluid mechanic fundamentals to arrive at a competitive heat exchanger geometry using low-thermal-conductivity materials like composite-polymers and stainless steels. First, a foundation is built for the manufacturing challenges and used to guide geometry development. Then the geometry is optimized using Computational Fluid Dynamics (CFD) models and heat exchanger thermal models around desired performance metrics. Various geometric and material combinations are printed and experimentally validated to benchmark modeling efforts and progress towards more complicated and intricate designs. The optimal proposed design is capable of transferring 8 kW at 40 Pa airside pressure drop with a face velocity 2.5 m/s and a 69.2°C temperature within difference 12" by 12" by 2" envelope.

Acknowledgements

Mom and Dad

Kasey

Greg

Sandy

Tom

SEL lab-mates and undergrads

ARPA-e

University of Wisconsin Grainger Institute and PEC

Table of Contents

Abstract 1
Acknowledgements 2
List of Figures 4
List of Tables 6
1 Introduction 7
2 Additive Design 12
3 Thermal Modeling 18
3.1 Airside Convection 20
3.2 Conduction 37
3.3 Waterside Convection 43
3.4 Thermal Modeling Conclusions 48
4 Experimental Validation 51
5 Conclusions 55
6 References 56
7 Appendix 57
7.1 Additive 57
7.1.1 3D Printers 57
7.1.2 Printed Heat Exchangers 57
7.2 Thermal 59
7.2.1 Microstructure CAD Drawings 59
7.2.2 Temperature Contours 61
7.3 Experimental 62
7.3.1 Test Loop Instrument Schematic 62
7.3.2 Test Loop Instrument Specifications 63
7.3.3 Test Loop Image 64
7.3.4 Kazoo Pressurization 65
7.3.5 Full-Scale Waterside Pressure Drop 67

List of Figures

Figure 1: HVAC standard copper tube and corrugated-aluminum fin heat exchanger 3
Figure 2: FDM nomenclature and hardware setup [sd3d.com]..... 4
Figure 3: Air-cooled cross-flow heat exchanger microstructure and macrostructure topology 6
Figure 4: Airfoil channel tool pathing (Top) Un-optimized tool path (Bottom) Optimized tool path..... 7
Figure 5: Tapered-pin fin continuous tool pathing and construction. 9
Figure 6: Solid and surface body modeling and resultant tool paths 10
Figure 7: Solid and surface body modeling applied to a full-scale heat exchanger..... 12
Figure 8: Microstructure geometries considered (Left) Airfoil (Middle) Tapered-pin (Right) Tapered ellipse fins. Reference Appendix Section 7.2.1 for detailed drawings. 13
Figure 9: Heat exchanger thermal resistance networks for solid and hollow fin types. 15
Figure 10: Thermal boundary layer convection analogous conduction length of $\delta_{t,\hat{x}}$ 17
Figure 11: As-modeled versus as-printed airfoil channel cross section..... 18
Figure 12: Velocity contours for pin-fin and airfoil-fin arrays..... 18
Figure 13: Tapered-ellipse evolution (Left) Constant cross section airfoil. (Middle) Tapered airfoil. (Right) Tapered ellipse. 19
Figure 14: Tapered Ellipse Geometry Definition..... 21
Figure 15: CFD computational domain and unit cell definitions..... 24
Figure 16: CFD mesh highlighting boundary layer, y+, and orthogonality concepts 25
Figure 17: Baseline DoE heat transfer rate vs airside pressure drop results..... 28
Figure 18: DoE 1 and DoE 2 heat transfer rate vs airside pressure drop results 30
Figure 19: DoE 1, DoE 2 and DoE 3 heat transfer rate vs airside pressure drop results..... 33
Figure 20: Polymer filler types: (Left) Carbon fiber (Middle) Printed nylon bead with short strand carbon fibers (Right) Aluminum flakes..... 34
Figure 21: Anisotropic thermal conductivity nomenclature 34
Figure 22: Fiber and flake filler content with process-dependent orientation as a results of the optimized airfoil microstructure tool path 36
Figure 23: Airfoil heat transfer rate as a function of wall thickness at varying isotropic and anisotropic thermal conductivities all optimized for a 12” x 12” heat exchanger at constant airside pressure drop. 37
Figure 24: Tapered-pin heat transfer rate as a function of thermal conductivity optimized for a 12” x 12” heat exchanger at constant airside pressure drop. 38
Figure 25: Waterside thermal and hydraulic case study setup..... 39
Figure 26: Fin efficiency as a function of waterside cavity depth at varying cavity thermal conductivities (analysis and figure credit: Mike Cheadle)..... 40
Figure 27: Waterside thermal gradient visualization with constant E at various values of H 42
Figure 28: Full-scale HX waterside flow distribution and pressure drop CFD..... 43
Figure 29: Optimal heat transfer rate for various geometry and material combinations at a fixed airside pressure drop 44
Figure 30: Heat exchanger heat transfer rate and average heat-transfer-coefficient for different geometry types and materials at face velocity u_f of 2.5 m/s and airside ΔP_a of 40 Pa. 46
Figure 31: Heat exchanger volume-weighted surface-area and volume for different geometry types and materials at face velocity u_f of 2.5 m/s and airside ΔP_a of 40 Pa. 47

Figure 32: Airfoil - Onyx air and waterside heat transfer rate data vs airside pressure drop data comparison to thermal model 50
Figure 33: Tapered-pin fin test results and models for three heat exchangers printed with three different materials. 50
Figure 34: Tapered ellipse as-printed heat exchangers 51
Figure 35: Tapered ellipse experimental test data and models for all three different waterside cavity cases 52
Figure 36: 3D printers used in this project. (Left) Makergear M2 (Middle) Makergear M2 heated enclosure (Right) EOS M 290 51
Figure 37: As-printed airfoil-onyx heat exchanger. Frontal area ~2.75" by 2.75" 51
Figure 38: As-printed tapered-pin heat exchangers for various materials 52
Figure 39: Printed heat exchanger graveyard 52
Figure 40: Airfoil Microstructure CAD drawing 53
Figure 41: Tapered-Pin Fin Microstructure CAD drawing 54
Figure 42: Tapered Ellipse Microstructure CAD drawing 55
Figure 43: Temperature contours of computational unit cell for Y =0 and Z =0 56
Figure 44: Temperature contours of computational unit cell for Y = 2 and Z = 1 56
Figure 45: Test loop instrument schematic 57
Figure 46: Image of test facility 59
Figure 47: Kazoo Pressurization DoE Setup and Results 60
Figure 48: Kazoo pressurization failure modes 61
Figure 49: Baseline full-scale waterside modeling and test results compared to maximum allowable pressure drop 62

List of Tables

Table 1: Heat exchanger project design requirements 5
Table 2: Tapered ellipse parametrized variables 20
Table 3: Baseline DoE Parameters 22
Table 4: Baseline DoE results for face velocity u = 2.5 m/s 27
Table 5: DoE 2 setup and results 29
Table 6: DoE 3 setup and results 31
Table 7: Anisotropic thermal conductivities for various filled materials [2] 35
Table 8: Waterside thermal and hydraulic results 41
Table 9: Test loop instrument specifications 56
Table 10: Kazoo pressurization DoE setup and results 60

1 Introduction

There has been increased hype surrounding the field of additive manufacturing and large efforts are ongoing that will allow the technology to evolve from one that is appropriate only for relatively high-cost prototypes to a production-worthy manufacturing process. The additive manufacturing process allows for unparalleled freedom in design and efficient use of material relative to traditional, subtractive manufacturing processes; however, additive manufacturing has historically been limited to low strength thermoplastics with inferior material properties and, due to low production rates, poor economics. Recent material and manufacturing developments have enabled printing of thermoplastic composites and metal parts at higher rates.

An application for additive manufacturing that is receiving much attention is heat exchangers. Heat exchangers are components that transfer thermal energy from one fluid to another with performance characteristics that are largely dependent on the geometric topology. Traditional heat exchangers use relatively simple geometries but are manufacturable at low cost. With additive manufacturing, more complex and potentially superior geometries are manufacturable offering the opportunity to solve an interesting engineering design problem.

Heat exchanger performance is characterized by the overall resistance to thermal energy transfer as a result of the geometry and how much fluid energy, or fluid pressure drop, is used to pay for it. For the air-to-water heat exchanger considered in this work, the generic formula for total resistance R_{total} given by:

$$R_{total} = R_{conv,a} + R_{cond} + R_{conv,w} = \frac{1}{\eta_f \bar{h}_a A_{s,a}} + \frac{t h_w}{k_m A_c} + \frac{1}{\bar{h}_w A_{s,w}} \tag{1}$$

Where $R_{conv,a}$ is the airside convection resistance, R_{cond} is the conduction resistance of the wall between the air and water, and $R_{conv,w}$ is the waterside convection resistance. Convection resistance is a function of wetted surface area A_s, a geometry and flow condition dependent heat transfer

coefficient $\overline{h}$, and fin efficiency η_f when extended surface are utilized. Conduction resistance is a function of wall thickness (th_w), material thermal conductivity (k_m), and cross-sectional area perpendicular to the direction of heat flow (A_c). To minimize thermal resistance, it is desirable to have high heat transfer coefficients, large amounts of surface area, thin walls, and a material with high thermal conductivity. As a result, small feature sizes are desirable. Small feature sizes yield thinner walls, larger amounts of surface area within a given volume, and typically lead to larger heat transfer coefficients.

The governing formula for pressure drop (ΔP) is given by:

$$\Delta P = \frac{1}{2} f \rho u^2 N \tag{2}$$

where f is a geometry and flow condition specific friction factor, ρ is the working fluid density, u is the fluid reference velocity, and N is a non-dimensional geometric relation typically defined as length over diameter in duct flow or number of fin rows in a fin array. With a set working fluid and operating condition, it is desirable to have low friction factors to minimize pressure drop. In convective heat transfer there commonly exists a coupled relationship between the geometry's heat transfer coefficient and friction factor; if a greater thermal performance is desired, it is also accompanied by an increased hydraulic penalty. From a designer's perspective, this behavior can be frustrating because it seems orders-of-magnitude easier to observe pressure drop increase exponentially with relatively little return on the heat transfer coefficient in a geometric optimization.

Air is a common working fluid in heat exchangers because most energy systems must ultimately reject or in some cases accept heat from atmosphere. Typically, the airside convection resistance is the largest limiting factor in overall performance due to low heat transfer coefficients related to the fluid's low density and low conductivity. Because of this, air-cooled heat exchangers are a prime candidate to be redesigned using the extra degrees of freedom enabled with additive manufacturing.

As a relevant first market for an additively manufactured heat exchanger adoption, the Heating Ventilation and Air Conditioning (HVAC) industry commonly uses air-cooled heat exchangers to condition building air or other integral working fluids like water and refrigerant. For such applications, these heat exchangers are commonly found in rooftop air-handling units and in building ductwork where large airflow rates must to pass through the heat exchanger with minimal pressure drop in order to condition building environments with minimal cost related to moving both working fluids. The industry standard in air-cooled heat exchangers is the copper-tube and corrugated-aluminum-fin cross-flow heat exchanger as shown in Figure 1. This technology is the product of many decades in engineering research and will serve as the benchmark in determining whether a family of additively manufactured heat exchangers is capable of being implemented into new HVAC product lines and accommodate retrofitting of existing systems. For an adoption to occur, a printed heat exchanger must have equal or better performance and economic metrics to that of the coils currently in use.

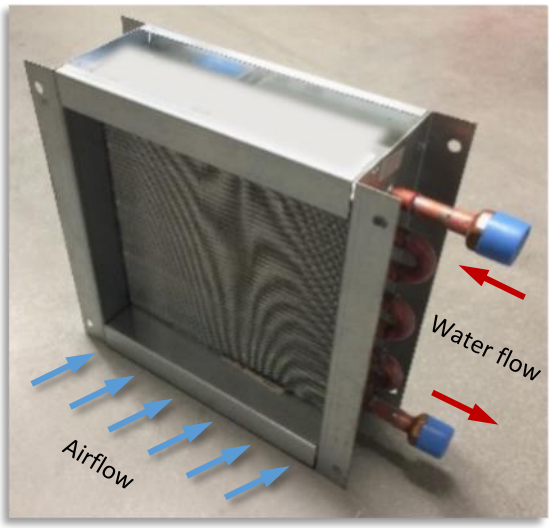

Figure 1: HVAC standard copper tube and corrugated-aluminum fin heat exchanger

In order to assure that an economically viable solution is reached, deposition based additive methods will be considered using composite polymers and stainless steel Metal Injection Molding (MIM) materials. MIM materials are composed of metal powders encased with polymer binders. To achieve a fully dense metal part with MIMs, a component is printed and then a sintering process melts away the binder and welds the metal powder particles.

Each material type presents two unique challenges on different ends of the spectrum. In the case of composite polymers, inexpensive materials and manufacturing hardware can be used but must

achieve performance metrics with materials having a thermal conductivity between 0.2 W/m-K and 1 W/m-K. These numbers being two orders of magnitude less than what is traditionally used in heat exchangers, aluminum and copper thermal conductivities are approximately 200 and 350 W/m-K respectively. Material strength and lifetime at operational temperature and pressure also present large uncertainties. In the case of stainless steel MIM materials, thermal conductivity is approximately 17 W/m-K and demonstrates superior material strength but more expensive material and manufacturing hardware is utilized.

Deposition additive processes, originally stemming from Stratasys' Fused Deposition Modeling (FDM), involves a tool head traversing a 2-dimensional x-y plane while extruding filament through a nozzle, melting it, depositing it, and growing the material as stacked 2D layers in the third or z-direction; as shown in Figure 2. Originally conducive to thermoplastics, companies like Markforged have adapted the technology to deposit MIM material and sinter parts in a post-processing step with what they refer to as Atomic Diffusion Additive Manufacturing (ADAM).

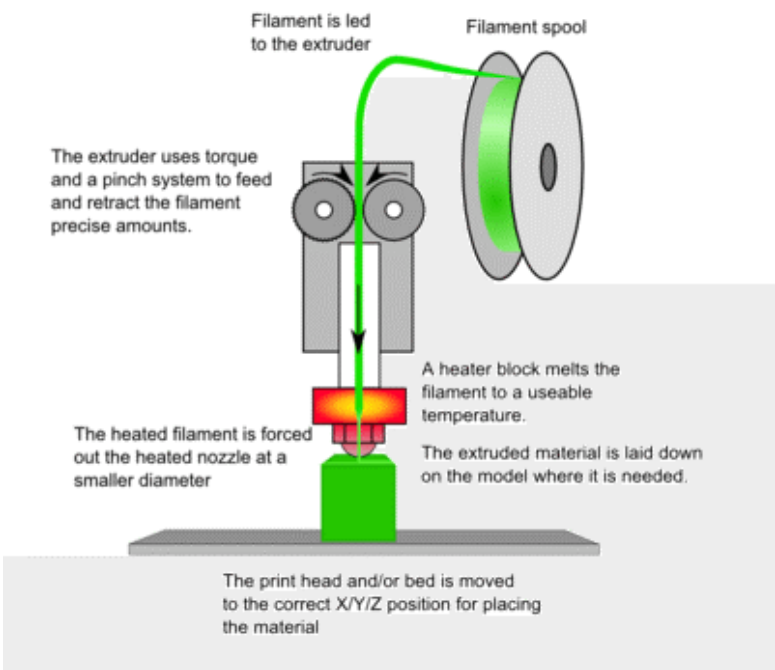

Figure2: FDM nomenclature and hardware setup [sd3d.com].

The following sections will focus on design considerations, performance modeling, and experimental validation of heat exchangers manufactured using deposition based additive manufacturing techniques with both composite polymer and stainless-steel materials. This work is application driven with the goal of servicing existing after-market heat exchanger applications as well as future product lines. Table 1 outlines the design requirements for the project. These metrics were provided through an industry source and are considered competitive with modern air-cooled heat exchanger technologies.

Table 1: Heat exchanger project design requirements

	Metric	Imperial
Heat exchanger envelope	304.8 mm x 304.8 mm x 50.8mm	12 in x 12 in x 2 in
Air flow rate (Velocity)	2.5 m/s	8.2 ft/s
Air flow rate (Volumetric)	0.23 m3/s	491 CFM
Water flow rate	1.6e-5 m3/s	9.6 LPM
Inlet air temperature	12.8 °C	55 °F
Inlet water temperature	82.2 °C	180 °F
Heat transfer rate	8 kW	27,297 BTU
Air side pressure drop	40 Pa	0.16 inH2o
Water side pressure drop	4.7 kPa	18.9 inH2o

In parallel to this heat exchanger work, collaborative research with the University of Wisconsin is being conducted in the follows areas:

- Thermally-conductive-composite-polymer filaments
- 17-4 SS MIM additive manufacturing and sintering processes
- Heat exchanger technology-to-market and economic analysis
- Performance of as-modeled vs as-printed microstructure heat transfer surfaces

2 Additive Design

The topology of the proposed additive heat exchanger is analogous to a flattened-tube heat exchanger. Figure 3 outlines the cross-flow fluid configurations, fluid distribution, heat exchanger microstructure, and macrostructure. The heat exchanger microstructure consists of a water channel, a wall, and an

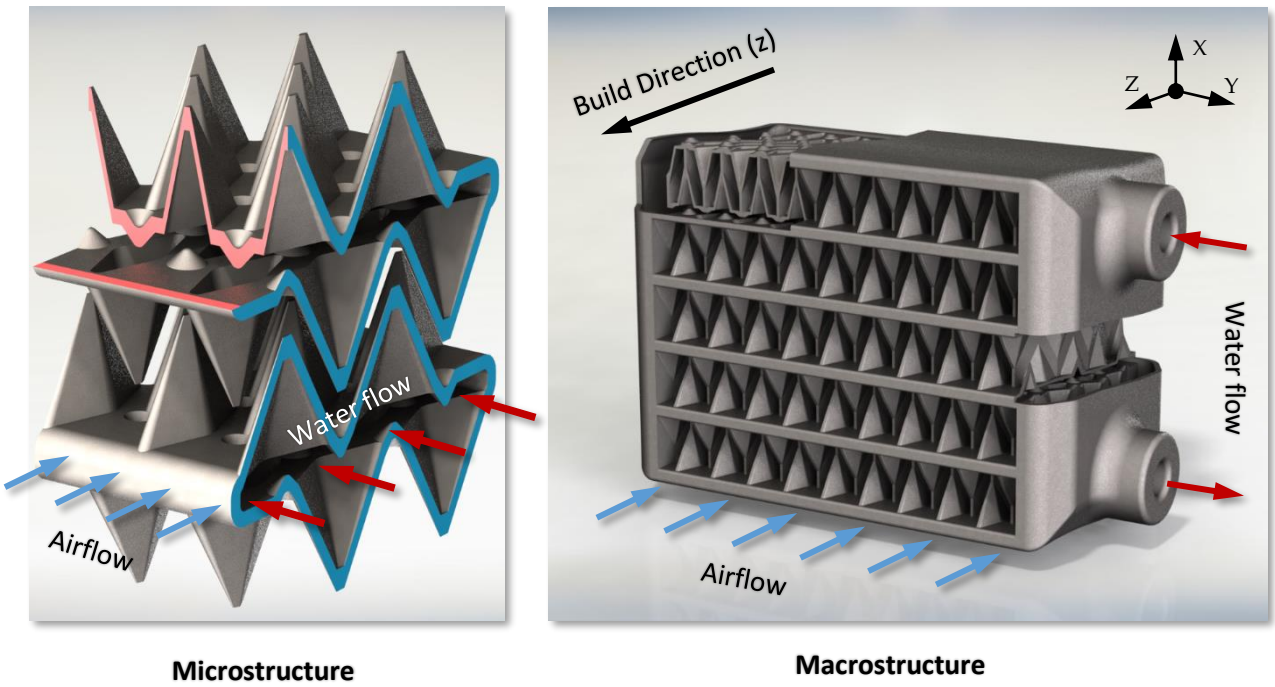

Figure 3: Air-cooled cross-flow heat exchanger microstructure and macrostructure topology

airside fin array. The design goal is to strategically place material within this microstructure to create non-traditional heat transfer surfaces enabled by additive manufacturing to achieve competitive performance metrics. Before arriving at the geometry shown in Figure 3, it is necessary to appreciate the fundamentals for manufacturing such small and intricate heat transfer surfaces using deposition based additive processes. Even though additive manufacturing allows for greater degrees-of-freedom in design, limitations still exist. Once a foundation of knowledge related to additive manufacturing and its constraints is obtained, Thermal Modeling Section 3 applies conduction and convective heat transfer fundamentals to arrive at a high performance and manufacturable geometry.

In the case of a heat exchanger, a printed component is considered a success if it is water tight at operational pressure and holds acceptable geometric tolerances. To accomplish these requirements, variables in the manufacturing processes are broken down into two groups: print parameters and tool pathing. Print parameters include standard items like deposition speed, layer height, extrusion temperature, retraction settings, etc. Tool pathing is more complex and is found to have a much larger effect on the water tightness of a printed part. Tool pathing can be thought of as the product of the geometry itself, how the geometry is modeled, how the geometry is exported from CAD software, and finally how the print head is controlled to deposit the material.

To illustrate these tool pathing ideas, a few baseline examples are used. First, consider the airside microstructure shown in Figure 4 featuring an airfoil fin and two corresponding tool paths generated with Simplify3D's slicing software. For the un-optimized tool path, a single solid body and thus a single process generates tool paths for the base-wall structure and fins. With the generic slicing algorithms, the varying path thickness exhibited in the geometry's layered cross sections leads to a deposition tool path with many travel moves (i.e., a discrete movement of the tool head not associated material deposition). The green and blue lines represent deposited material in the current or previous layers and the red lines represent tool head travel movements between perimeter start and end

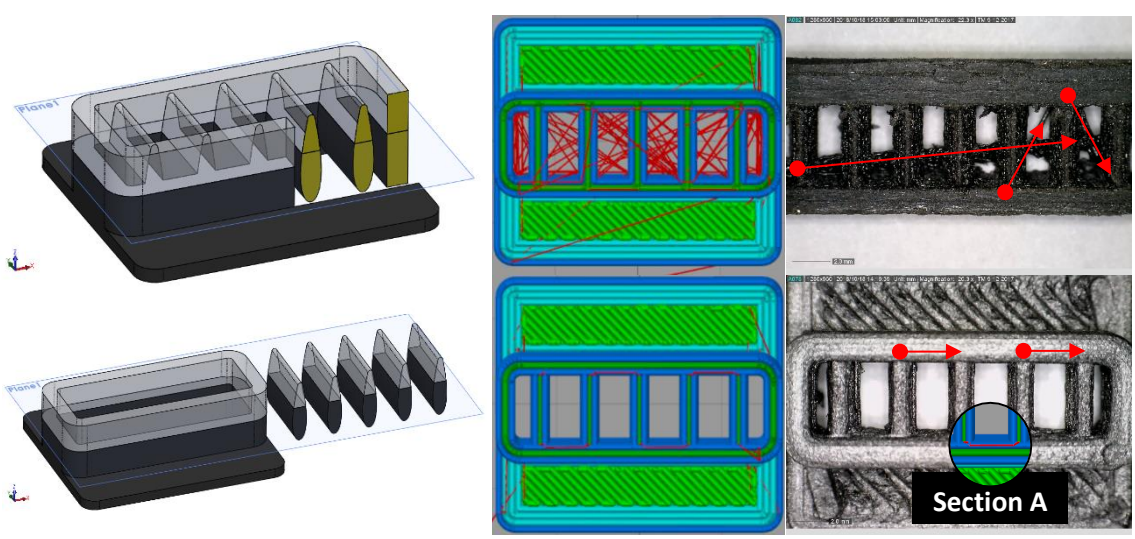

Figure 4: Airfoil channel tool pathing (Top) Un-optimized tool path (Bottom) Optimized tool path

locations. These (red) travel movements lead to barnacle-like build up on printed features affecting geometric integrity and eventually interfering with watertight perimeters. To remove these defects, unnecessary tool head movements are optimized by treating the base-wall structure and fins as two independent processes resulting in sequential printing of the two features. This change, along with a handful of other slicer settings, help to preferentially guide movements between features and between layers to aid in minimizing travel moves. However, due to the varying thickness of the airfoil geometry, a discontinuity will always exist for features of this nature. The optimized tool path results in an part with acceptable geometric tolerances but, while subtle, a travel move still exists at Figure 4 Section A.

Appendix Kazoo Pressurization Section 7.3.4 quantitatively characterizes the water tightness effects of this break in the material deposition process. In the study, two common modes of failure are observed, first at an external wall and second at the fin seam highlighted in at Section A. The first is attributed to improper print parameters but the second is attributed to the discontinuity in tool path at this fin-wall junction. Also for the latter, samples frequently failed to hold water above even 1 psi; desired burst pressures for are upwards of a few hundred psi.

Initial printing and pressurization trials of intricate geometries like the airfoil indicated that optimal tool paths exhibit minimal travel movements and minimal discontinuities in material deposition. To maximize continuity, consider the airside microstructure as shown in Figure 5 featuring a tapered-pin fin and four corresponding tool paths. At Layer A, the tool head “bumps” out from the wall creating the base of the fin all while continuously moving in the wall direction. This bump is small enough that the material welds well to the previous layer but large enough such that it provides Layer B with enough support to create a larger bump in the following layers; this process continues layer-by-layer to generate a tapered fin structure. This continuous deposition process allows material to grow out from the top and bottom walls, eventually forming the fin observed in Layer C. From Layer C onwards, tool pathing repeats as a mirror image of the previous layers until complete, as shown in Layer D. In every layer of

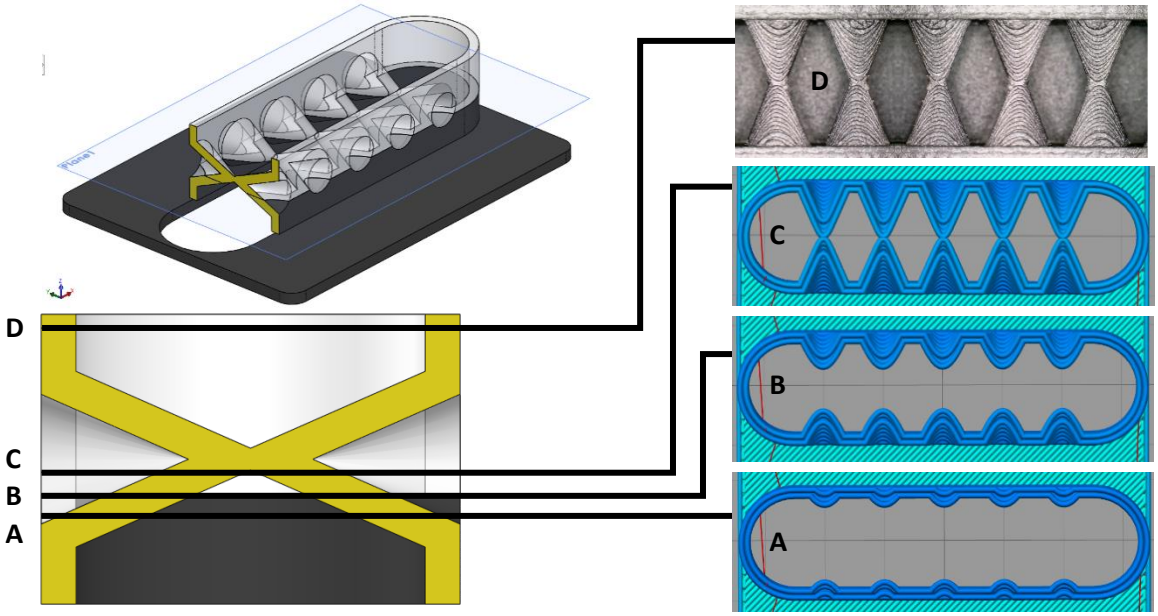

Figure 5: Tapered-pin fin continuous tool pathing and construction.

this geometry, each tool path has one starting and one ending position enabling continuous material deposition. Instead of a discontinuity in material flow existing at every fin and in every layer as observed with the airfoil geometry, there now exists only one discontinuity at layer change. This allows for faster print times and in a full-scale heat exchanger with thousands of fins, this reduction in discontinuity ultimately leads to a higher success rate of watertight parts. While an in-depth study was not conducted on tapered-geometry water tightness, numerous samples exceeded 100-psi burst pressure and displayed no common modes of failure.

With overarching objective of creating continuous tool paths for an additively manufactured heat exchanger having been identified, creating three-dimensional geometries with a constant cross-section in each sliced layer becomes both a design and a CAD challenge. To reach this goal, a combination of solid-body and surface-body modeling techniques are used. It is a well-known practice to model geometries using solid bosses and use STL file formatting for slicing software to generate tool paths. The issue with solid bodies and continuous tool pathing is the difficulty in perfectly tailoring every sliced layer in the build direction to the tool head being used. On the other hand, CAD surface

body STLs are sliced and interpreted as a vector for the tool head to follow with the amount of material deposited dependent on extrusion multiplier thus removing the difficulties observed using solids. To illustrate the benefit of surface modeling, consider the tapered pin shown in Figure 6, a single fin at Layer B of Figure 5. The solid body example provided is an exaggeration but representative of two common issues when designing and manufacturing a feature with the thickness of a single nozzle diameter. First, the base of the fin has a discontinuity due to an area constriction. Second, the tip of the fin shows the deposition of two beads due to an area expansion. Adding material to the base and cutting away material from the core resolves these issues and successfully creates a manufacturable heat exchanger. However, as geometries and tool pathing get more complex, these minor adjustments quickly become tedious and cumbersome and switching to a surface modeling technique removes all need for any such adjustments. The surface body shown in the Figure 4 is the same external surface

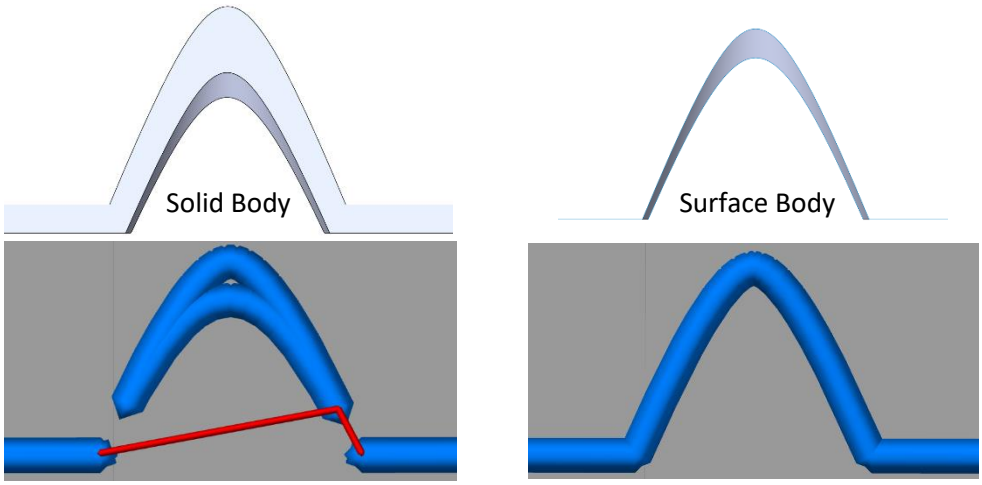

Figure 6: Solid and surface body modeling and resultant tool paths

used in the solid body but the tool path result is continuous.

Extrapolating these manufacturing concepts to a full-scale heat exchanger, surface-bodies are used to represent critical features like fins and thin walls where a continuous watertight seal is needed. Solid bodies are used to represent areas where small discontinuities in tool path have negligible impact on water-tightness. This includes areas like outer channel walls and headers where thicker walls and

thus multiple perimeters can be used to seal channels. This concept of different modeling techniques for different features all comes together in Figure 7. In a layer-by-layer fashion, the tool head deposits material for the surface bodies or fins in one continuous loop (Process 1) and then deposits material for the solid bodies (Process 2). While significantly different print parameters are defined for each process,

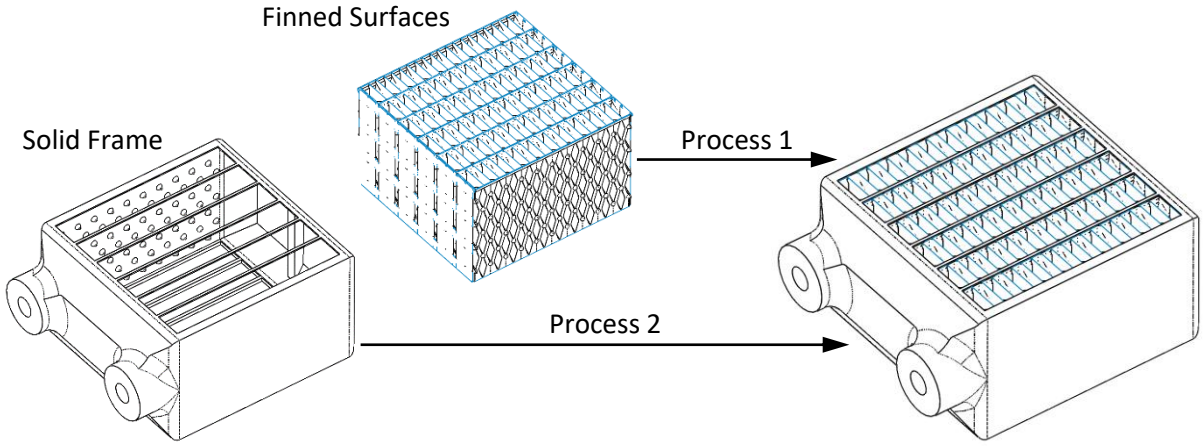

Figure 7: Solid and surface body modeling applied to a full-scale heat exchanger

both come together to yield a single part.

While potential value exists in writing a unique slicer software or in modeling one surface to include the heat exchanger fins and frame to create one continuous printing process, manufacturing preparation was focused on manipulating existing software while minimizing CAD complexity in order to allow as significant focus on developing the geometries shown. In the next section, fundamentals of heat transfer and fluid dynamics are coupled with these manufacturing constraints to develop a performance competitive geometry.

3 Thermal Modeling

Heat exchanger thermal and hydraulic performance models utilize CFD correlations and the $\varepsilon - NTU$ method with total resistance to heat transfer as the conceptual model driving development. For this analysis, consider the three fin geometries and their orientation to the microstructure as shown in Figure 8, an airfoil fin with constant cross section, a hollow tapered pin-fin, and a hollow tapered elliptic-fin with waterside structure. Airside heat transfer coefficient and friction factor correlations for the airfoil geometry shown can be found in Rachel Felber's Master's thesis [3] and similar information for the tapered pin-fin geometry in Courtney Leed's Master's thesis [4]. This work attempts to combine the advantageous features of these two geometries to develop a hybrid tapered-elliptic geometry that is manufacturable and performs competitively while making efficient use the material mass required.

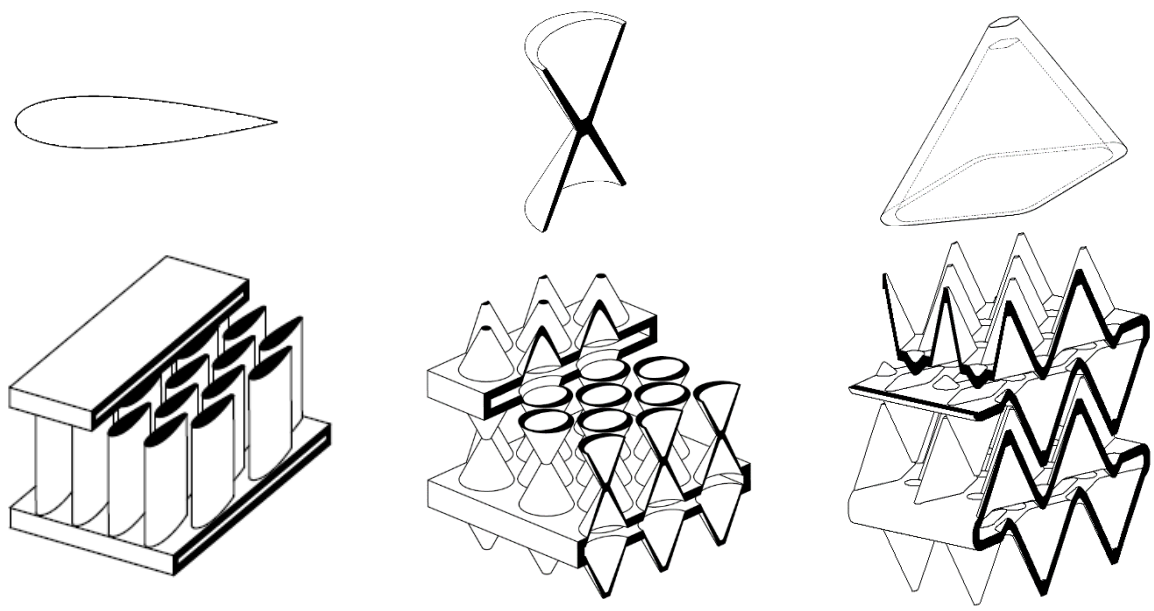

Figure 8: Microstructure geometries considered (Left) Airfoil (Middle) Tapered-pin (Right) Tapered ellipse fins. Reference Appendix Section 7.2.1 for detailed drawings.

The two thermal resistance networks for each type of geometry being investigated are outlined in Figure 9, one for the solid airfoil and the other for the hollow-tapered geometries. The difference between the resistance networks is that the solid airfoil utilizes extended surface fin efficiencies and the hollow tapered geometries do not, resulting in an overall shorter length of conduction. This behavior is especially beneficially for materials having lower thermal conductivities, like polymer and stainless steel.

Both resistance networks can be broken down into three groups: airside convection resistance, conduction resistance, and waterside convection resistance. The following sections investigate these

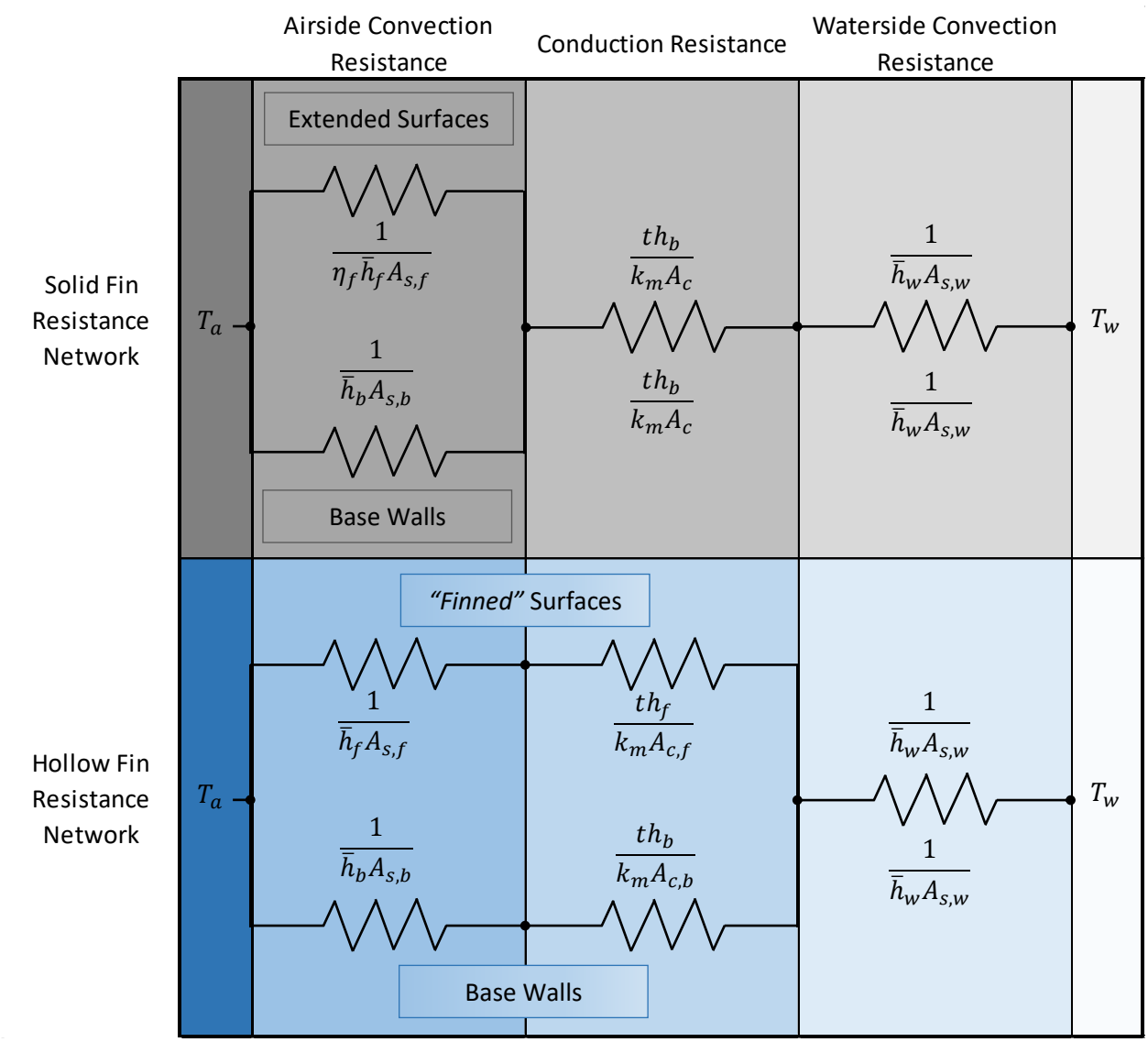

Figure 9: Heat exchanger thermal resistance networks for solid and hollow fin types.

resistances and utilize first principles in heat transfer and fluid mechanics to optimize thermal and hydraulic behavior.

3.1 Airside Convection

Convection resistance is a result of the heat transfer coefficient $\bar{h}$ and surface area A_s associated with a geometry. For an extended surface, convection resistance is given by:

$$R_{conv} = \frac{1}{\eta_f \, \bar{h} \, A_s} \tag{3}$$

where η_f is the fin efficiency, a ratio of fin heat transfer to an ideal fin heat transfer. An ideal fin maintains constant temperature throughout that is equal to that of the base temperature. For materials with low conductivity, this requirement can only be approximately met if the conduction length along the fin is short, resulting in short fins and increased airside flow restriction. For the hollow tapered geometries where extended surfaces are not utilized, convection resistance is given by:

$$R_{conv} = \frac{1}{\bar{h} \, A_s} \tag{4}$$

the removal of the fin efficiency from convection resistance allows airside structure to extend further into the free stream, which opens up the frontal area of the heat exchanger; this requires that waterside structures are present so that water flows in-to and out-of the hollow fin core. Section 3.3 investigates such waterside structure.

To reduce convection resistance in both cases, increasing surface area is an easy solution but not always possible given mass and volume constraints. Increasing the heat transfer coefficient is the other possible solution but more difficult to accomplish given the geometry and flow-condition dependence. At a conceptual level, a simpler heat transfer mode is used to understand this dependence - conduction. Convective heat transfer reduces in some sense to a conduction problem within a thermal boundary layer; instead of heat transferring due to interactions between energy carriers within a material, heat transfers due to interactions between fluid molecules. In conduction, it is well known and

understood that a thinner wall or shorter conduction path is less resistive to heat transfer. In convection, this length is analogous to the thermal boundary layer thickness. Consider flow over the heated surface shown in Figure 10, the surface temperature T_s, thermal boundary layer δ_t, and free

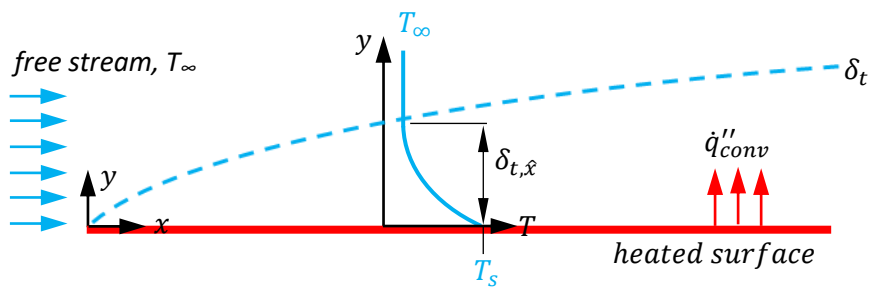

Figure 10: Thermal boundary layer convection analogous conduction length of $\delta_{t,\hat{x}}$

stream temperature T_∞. Using Fourier's Law and the conduction analogy, equation 5 shows the rate of convective heat flux that passes through the surface and into the fluid is proportional to the boundary layer thickness over the fluid thermal conductivity k_f or the inverse of the heat transfer coefficient [1]. Thus with set fluid and flow conditions, a thin boundary layer minimizes convection resistance.

$$\dot{q}''_{conv} \approx -k_f \left.\frac{\partial T}{\partial y}\right|_{y=0} \approx k_f \frac{(T_\infty - T_s)}{\delta_t} \approx \bar{h}(T_\infty - T_s) \tag{5}$$

To apply this concept in a heat exchanger geometry, the fin banks shown in Figure 8 redevelop boundary layers at each individual fin and therefore thermal optimization leads to many small fins. With the chosen manufacturing process, feature size is limited by the deposition nozzle diameter, typically around 0.5mm. For example, Figure 11 shows an as-modeled versus an as-printed airfoil fin comparison with diameter of 1.3mm and cord length of 5.4mm. The as-printed result is a digital representation of the as-modeled feature and therefore to achieve acceptable feature resolution, minimum feature sizes are required to be a few times that of the nozzle diameter. This digital result poses the interesting question about the impact on the boundary layer, heat transfer coefficient, and friction factor associated with this wavy or bumpy surface. These phenomena are investigated in Cassandra Wright's Master's Thesis [5] but in short can be summarized by the following statements. Within the HVAC heat

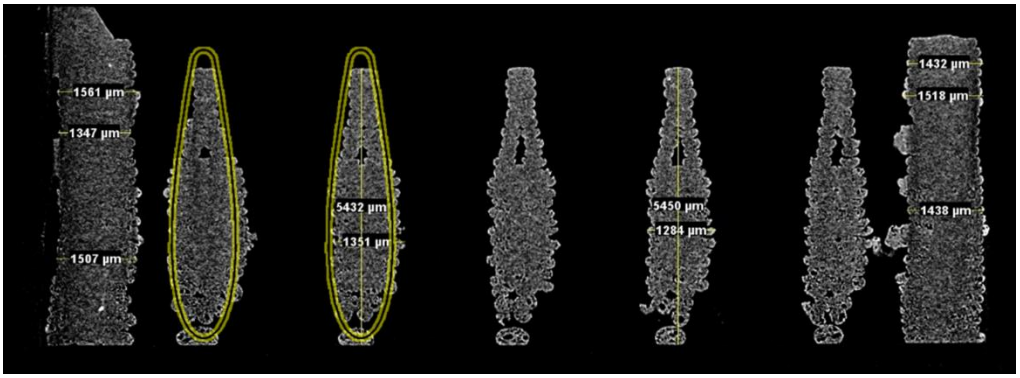

Figure 11: As-modeled versus as-printed airfoil channel cross section.

exchanger operating regime of Reynolds numbers below 1000, as the surface strays from smooth to bumpy, the friction factor increases at the surface and the heat transfer coefficient decreases. However, for this reduction in thermal/hydraulic performance there is an offsetting decrease in thermal resistance due to an increase in surface area. With experimental data to validate this behavior, all airside modeling assumes smooth surfaces for simplicity and computational ease.

The concept for reducing convection resistance by using tapered, elliptic hollow fins must be achieved while mitigating airside pressure drop, governed by friction and form drag. Friction drag is inherently involved with flow over the surface of these features but the more significant effect on pressure loss observed in the proposed fin arrays is related to form drag. Form drag is caused by separation of the boundary resulting in a low-pressure wake region downstream the fin.

Consider velocity contours for the pin fin and airfoil arrays shown in Figure 12. The pin fin flow separates leaving a wake region downstream. The high stagnation pressure at the leading edge and low-pressure region at the trailing edge results in a drag force exerted on the fin and thus fluid pressure

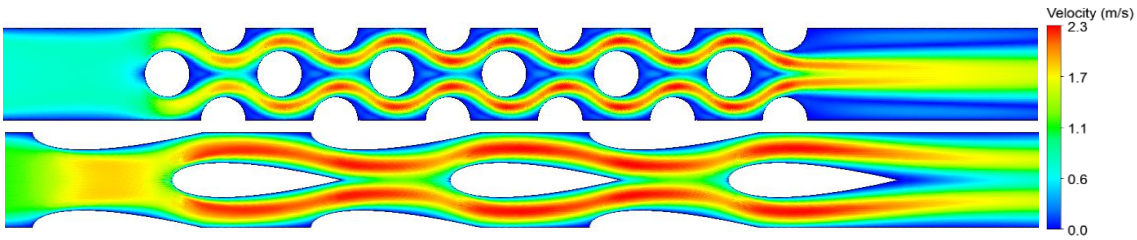

Figure 12: Velocity contours for pin-fin and airfoil-fin arrays

loss. These form drag effects are often much larger than those associated with friction drag and when designing for applications like HVAC with little allowable pressure drop, streamlined geometries are optimal and required for minimizing form drag. The airfoil is a good example of such streamlined geometry. As observed in Figure 12, minimal wake regions in the airfoil geometry exist. The average pressure loss per fin in the pin and airfoil fin arrays shown are 12 and 7 Pa/fin respectfully.

The average heat-transfer-coefficients for the pin and airfoil fins are 150 and 79 W/m2-K respectfully. Note that in this simple example, an increase in heat transfer coefficient is accompanied by increased pressure drop. Two additional metrics used to characterize heat exchangers are surface-area to volume (m^2/m^3) and mass to volume (kg/m^3) ratios. As there is a coupled relationship with surface-area, mass, thermal performance, and pressure drop, these metrics will be revisited in Thermal Modeling Conclusions Section 3.4

The airfoil array demonstrates acceptable hydraulic and thermal behavior but has poor manufacturability with the chosen deposition process and is a heavy geometry due to the constant cross-section and therefore large amount of mass required to construct each fin. On the other hand, the tapered-pin array demonstrates exceptional thermal behavior and manufacturability due to the tapered and on-average smaller diameters. However, it has poor hydraulic behavior due to the shape induced form drag. An obvious hybrid geometry between these two is tapering the airfoil as shown in Figure 13. The tapered airfoil maintains similar behavior to that of the straight airfoil and therefore

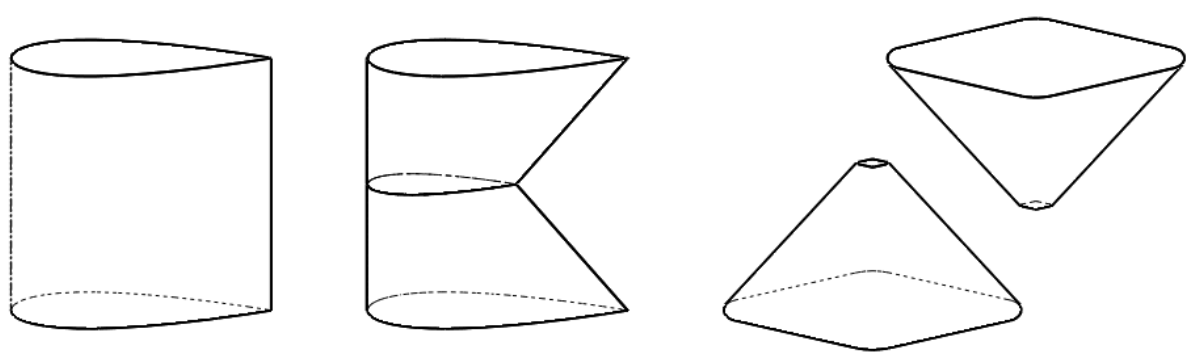

Figure 13: Tapered-ellipse evolution (Left) Constant cross section airfoil. (Middle) Tapered airfoil. (Right) Tapered ellipse.

enables the continuous deposition tool path. However, this removal of fin mass leads to a removal of surface area within the same volume. To maximize the surface-area to volume ratio, the tapered airfoil is decoupled at the fin center, shifted, and the two halves morphed to create a well-meshing tapered ellipse fin-array geometry.

At a conceptual level, the tapered ellipse makes a lot of sense. It regularly redevelops boundary layers, is streamlined, and allows for a continuous deposition tool path thus fulfilling thermal, hydraulic, and manufacturability requirements. To optimize the geometry and achieve performance metrics, the geometry is parametrized in accordance to Table 2 and Figure 14, and CFD simulations are run to extrapolate relevant heat transfer coefficients and friction factors.

Table 2: Tapered Ellipse Parametrized Variables

Parameter	Description
db_1	Fin first base diameter
a	Fin first base radius ($db_1/2$)
db_2	Fin second base diameter
b	Fin second base radius ($db_2/2$)
c_f	Fin height
dt_1	Fin first tip diameter
dt_2	Fin second tip diameter
α	Fin overhang angle
c_o	Fin overlap percentage
c_c	Air channel height
S_T	Fin array transverse pitch
S_L	Fin array longitudinal pitch
y	Sinusoidal array offset in transverse direction
z	Sinusoidal array offset in longitudinal direction
E	Non-dimensional base diameter ratio (b/a)
H	Non-dimensional fin height (c_f/b)
C	Non-dimensional fin overlap (c_o/c_f)
ST	Non-dimensional fin array transverse pitch (S_T/db_1)
SL	Non-dimensional fin array longitudinal pitch (S_L/db_2)
Y	Non-dimensional array offset (y/b)
Z	Non-dimensional array offset (z/c)

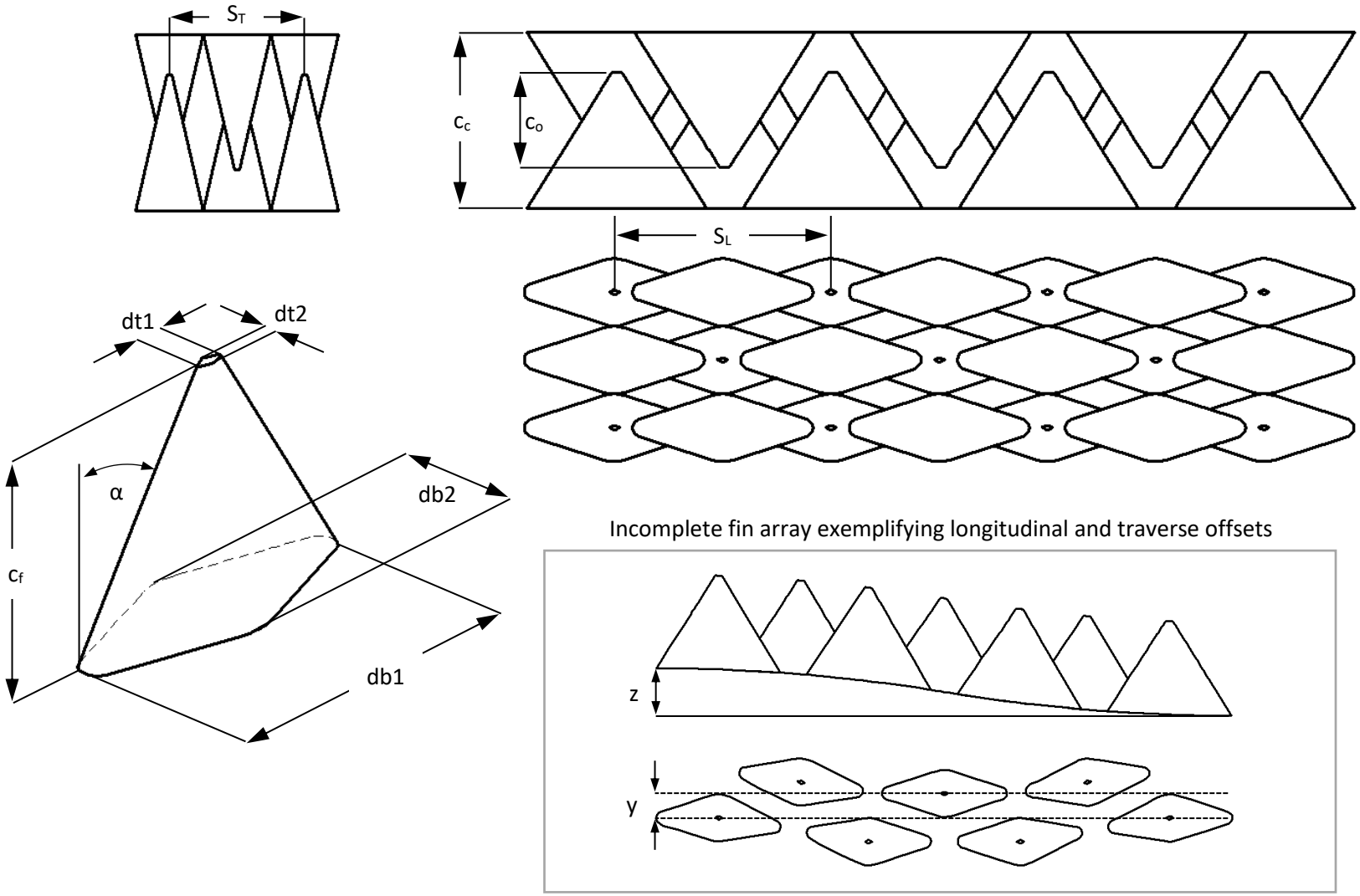

Figure 14: Tapered Ellipse Geometry Definition

Rather than develop comprehensive correlations using appropriately defined dimensionless parameters for every Degree-of-Freedom (DoF) over a large range of flow conditions, an incremental optimization approach around the target performance metrics is taken. Using existing correlations for the airfoils and tapered-pin fins, fin efficiencies, and manufacturing constraints, dimensional and non-dimensional baselines for DoFs were approximately established. From this baseline, Designs-of-Experiments (DoE) and DoF Main Effects (ME) are gauged as having either a positive or a negative impact on performance. At which point an incremental step is made towards the performance goal. After repetition and approach of the goal, a second approach is used. The University of Wisconsin's Center High Performance Computing (HPC) cluster is utilized to take advantage of modern computing power to quickly simulate numerous geometry combinations already established as having high potential. The following sub-sections describe simulating the baseline geometry, the incremental steps taken, and optimization with the HPC cluster.

The non-dimensional baseline values for the first baseline geometry are outlined in Table 3.

Table 3: Baseline DoE Parameters

Parameter	Low	Average	High
Fin Base Eccentricity, E_b (-)	0.20	0.25	0.30
Fin Top Eccentricity, E_t (-)	0.30	0.65	1.00
Fin Height, H (-)	11.00	13.50	16.00
Fin Overlap, C_o (-)	0.40	0.60	0.80
Transverse Pitch, S_T (-)	1.80	1.90	2.00
Longitudinal Pitch, S_L (-)	0.50	0.65	0.80

Justifications for the relations and values are as follows:

- Fin base eccentricity: lower base fin eccentricity results in a more streamlined geometry but too low results in manufacturing challenges and waterside cavity stagnation (To be investigated in Waterside Convection Section 3.3)

- Fin top eccentricity: lower tip eccentricity results in a more streamlined geometry but too low results in manufacturing overhang challenges with minimum values constrained by the deposition nozzle
- Fin height: larger fin heights result in a more open airside geometry but lower fin efficiencies
- Fin overlap: Larger fin overlaps result in a larger surface-area to volume (m^2/m^3) ratio but constricts the airside geometry resulting in a larger pressure drop.
- Pitch values: In an effort to maximize surface-area and minimize volume (m^2/m^3), longitudinal pitch is optimal at lower values and transverse pitch optimal at higher values

The process workflow for simulating the geometry begins with extracting a computational unit cell representative of the airside geometry. The next step includes generating a mesh that is consistent with the airside flow Reynolds regime. The final step, simulating the unit cell in ANSYS Fluent and extracting the heat transfer coefficient and friction factor for use in a full-scale 12” by 12” heat exchanger thermal model. Each one of these steps is conducted per unique geometric combination. To minimize time-consuming and tedious clicking involved with modeling and meshing each geometry, this part of the process is automated using a well-defined parametric CAD model and the mutual link between SolidWorks and ANSYS Workbench (Reference: Parametric Best Practices – ANSYS e-Learning).

The selected computational domain takes advantage of existing symmetry conditions within the fin array to minimize computation power and time required for simulation. Inlet and outlet air-blocks are also added to aid in minimizing entrance and exit effects that exist in numerical simulation. Figure 15 shows such computational domain and relevant boundary conditions.

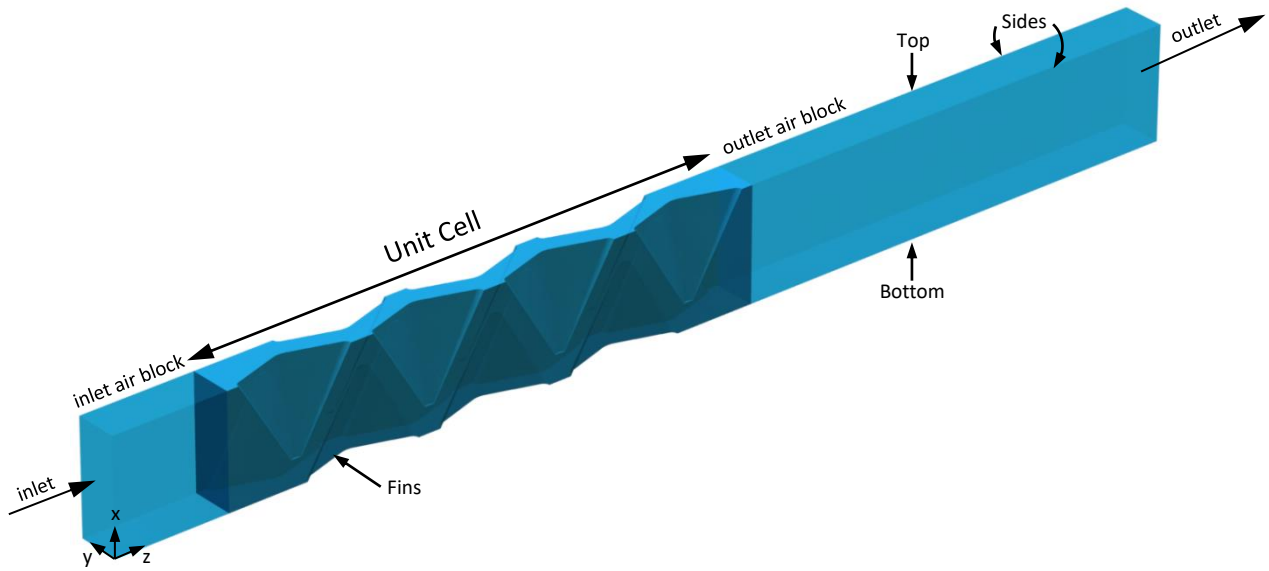

Figure 15: CFD computational domain and unit cell definitions

Boundary conditions for the CFD computational domain are as follows:

- Inlet: Velocity and Temperature
- Outlet: Pressure
- Finned Surfaces: Surface Temperature
- Unit Cell Top and Bottom: Surface Temperature
- Unit Cell Sides: Symmetry
- Air Block Top and Bottom: Symmetry
- Air Block Sides: Symmetry

Before generating a mesh, it is important to understand the flow regime and the behavior of the geometry being simulated. With flow conditions in the laminar regime and flow separation likely to occur with some geometric combination, the $SST\ k-\omega$ turbulence model is used in simulation because it is well-known for yielding accurate solutions near wall boundaries and accurately predicting pressure gradients in flow separation. With the $SST\ k-\omega$ model in mind, it is appropriate to begin

thinking about the mesh. For this model optimal mesh y^+ values are equal to 1. y^+ is a non-dimensional distance used to describe the mesh quality near the wall of the simulation flow field and is given by:

$$y^+ = \frac{yu^*}{\nu} = \frac{\Delta s u^*}{\nu} \tag{6}$$

Where Δs is the size of the first element at the wall, u^* is the friction velocity, and υ is the fluid kinematic viscosity. For a Reynolds number of 1000, the resultant Δs is approximately 0.07 mm. Figure 16 applies y^+ concepts to a 2D mesh at the top of the computational domain. From the first element at the wall, the mesh is gradually inflated into the free stream to accurately capture boundary layer effects. This meshing approach is generically applied to variations in the geometry and in three dimensions throughout the mesh automation process. With automation and mass generation of meshes,

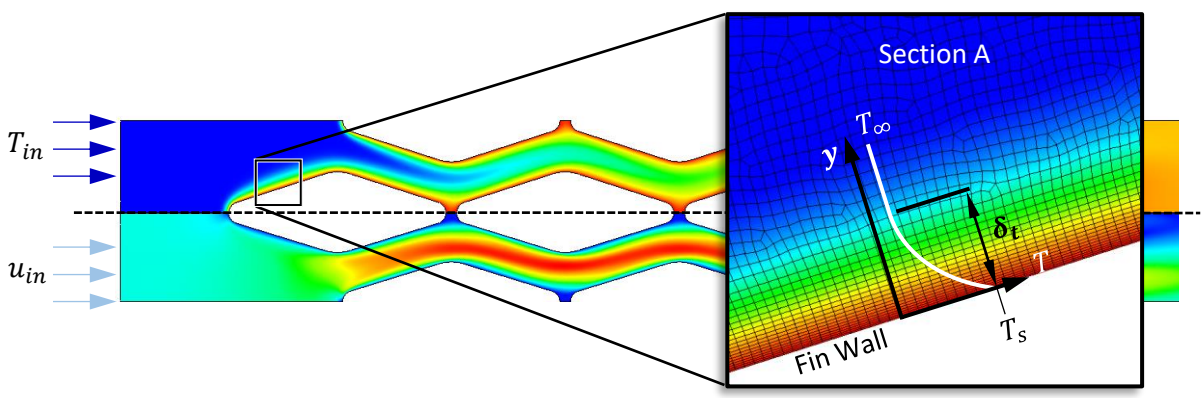

Figure 16: CFD mesh highlighting boundary layer, y^+, and orthogonality concepts

orthogonal quality is the mesh metric used for quality control. The range for orthogonal quality is 0-1; 0 being the worst and 1 being the ideal element. In layman's terms, an ideal element is one with uniform shape; for example an equilateral triangle or a perfect square. An element with low orthogonal quality would be a long and short parallelogram. In a three-dimensional mesh, minimal orthogonal quality is required to be above 0.1 with average values near 0.8 for simulation convergence and accurate results.

To verify meshing the meshing strategy and establish grid independence, a mesh element-number study was conducted on inlet pressure and outlet temperature parameters. Depending on DoF dimensional values, each mesh requires between two and four million elements.

After mesh generation, the geometry is imported into ANSYS Fluent, where a journal file is used to define solving methods, fluid properties, boundary conditions, convergence criteria, etc. In short, the file contains all the information needed to import a mesh into Fluent, conduct the simulation, and export the relevant information needed to extract the geometry's heat transfer coefficient and friction factor. The average heat-transfer coefficient $\bar{h}$ is found using the $\varepsilon - NTU$ method [1]. The effectiveness ε of the geometry is defined as:

$$\varepsilon = \frac{T_{out} - T_{in}}{T_s - T_{in}} \tag{7}$$

where T_{out} and T_{in} are the bulk temperatures at the computational domain outlet and inlet and T_s is the temperature of the fin surfaces. The number of transfer units NTU is defined as:

$$NTU = -\ln(1 - \varepsilon) \tag{8}$$

The result for NTU is then used to find the average heat transfer coefficient $\bar{h}$ in Equation 9. Where $\dot{m}$ is the fluid mass flow rate, $c_p$is the fluid's specific heat, and $A_s$is the heated surface area.

$$\bar{h} = \frac{\dot{m} c_p NTU}{A_s} \tag{9}$$

The friction factor f is found using equation 10. Where P_{in} and P_{out} are the simulation pressures at the computational domain inlet and outlet, ρ is the fluid density, $u_{in}$is the inlet velocity, and $N_L$is the number of fin rows in the longitudinal direction.

$$f = 2\frac{P_{in} - P_{out}}{\rho u_{in}^2 N_L} \tag{10}$$

Using the heat transfer coefficient and friction factor from the unit cell in conjunction with the hollow-fin thermal resistance network from Figure 9,the full scale 12” by 12” heat exchanger heat transfer rate and pressure drop are calculated also using the $\varepsilon - NTU$ method. The main effects on each performance metric are then computed by: The main effects for heat transfer rate given by:

$$ME_{E_b} = \frac{\sum_{i=1}^{n} \pm \dot{q}}{n} \tag{11}$$

where ME_{E_b} is the Base Eccentricity Main Effect, n is the number of geometry combinations, $\dot{q}$ is the thermal model heat transfer rate, and $\pm$ corresponds to a positive or negative multiplier depending on a high or low value in the DoE.

This process outlines the general simulation workflow from starting with CAD geometry to evaluating its thermal and hydraulic performance. This process is repeated for three flow conditions, heat exchanger face velocity u equal to 1.5, 2.5, and 3.5 m/s, with every geometry combination in the DoE. Table 4 shows the results from this DoE.

Table 4: Baseline DoE results for face velocity u = 2.5 m/s

Parameter	Low	Avg.	High	Pressure Drop (Pa)		Heat Transfer Rate (kW)	
				Main Effect	Normalized	Main Effect	Normalized
Fin Base Eccentricity, E_b (-)	0.20	0.25	0.30	0.33	0.04	-0.57	-1.00
Fin Top Eccentricity, E_t (-)	0.30	0.65	1.00	-0.55	-0.07	-0.11	-0.19
Fin Height, H (-)	11.0	13.5	16.0	2.63	0.34	-0.41	-0.72
Fin Overlap, C_o (-)	0.40	0.60	0.80	6.38	0.81	0.35	0.62
Transverse Pitch, S_T (-)	1.80	1.90	2.00	-6.00	-0.76	-0.22	-0.39
Longitudinal Pitch, S_L (-)	0.50	0.65	0.80	-7.84	-1.00	0.22	0.38

These results are interpreted with the following:

- As E_b increases from 0.25 to 0.30, $\dot{q}$ decreases by 570 Watts and ΔP increases by 0.33 Pascal.
- As E_t increases from 0.65 to 1.00, $\dot{q}$ decreases by 110 Watts and ΔP decreases by 0.55 Pascal.
- As H increases from 13.5 to 16, $\dot{q}$ decreases by 410 Watts and ΔP decreases by 2.63 Pascal
- As C_o increases from 0.60 to 0.80, $\dot{q}$ increases by 350 Watts and ΔP increases by 6.38 Pascal

- As S_T increases from 1.90 to 2.00, $\dot{q}$ decreases by 220 Watts and ΔP decreases by 6 Pascal
- As S_L increases from 0.65 to 0.80, $\dot{q}$ increases 220 Watts and ΔP decreases 7.84 Pascal

Table 5 also shows normalized ME values. Normalized ME values of 1.00 signify the most influential parameter on a performance metric. For example, base eccentricity E_b has the largest effect on heat transfer rate and longitudinal pitch S_L has the largest effect on pressure drop. The ME values tell which DoF are important and how a geometry is to respond to a DoF perturbation. Using these values with the raw heat transfer rate and pressure drop data points as shown in Figure 17, DoFs are incrementally changed such that movements toward the target are made. Again, Figure 17 shows heat transfer rate vs airside pressure drop from the thermal model results for each flow condition and geometric combination in this DoE. Also highlighted in this figure is the target heat transfer rate and pressure drop

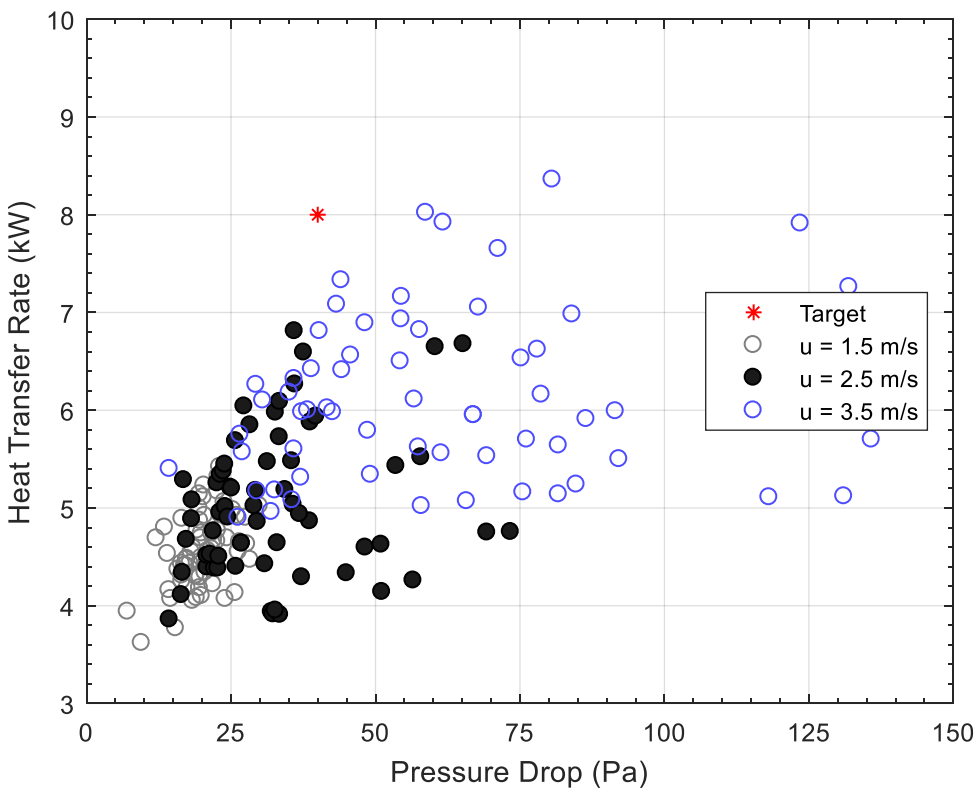

Figure 17: Baseline DoE heat transfer rate vs airside pressure drop results

at heat exchanger face velocity of 2.5 m/s. With the majority of data points falling short of the target heat-transfer rate, it is obvious that the next steps to be taken should aim at closing this gap.

The next DoE centers around fin base eccentricity, fin height, and fin overlap; the three most influential parameters on heat transfer rate from DoE 1. Table 5 outlines the increments made with each variable and the results from the analysis.

Table 5: DoE 2 setup and results

Parameter	Low	Avg.	High	Pressure Drop (Pa)		Heat Transfer Rate (kW)	
				Main Effect	Normalized	Main Effect	Normalized
Fin Base Eccentricity, E_b (-)	0.15	0.18	0.20	0.93	0.15	-0.32	-0.65
Fin Height, H (-)	8	9	10	-6.39	-1.00	-0.49	-1.00
Fin Overlap, C_o (-)	0.75	0.83	0.90	5.05	0.79	0.05	0.10

Analyzing the normalized heat transfer values, the following conclusions are made for each parameter:

- Base eccentricity has gone from being the most influential parameter to being dominated by fin height suggesting that an optimal value exists between 0.15 and 0.18. However at these values, waterside cavity stagnation remains an issue and larger values will continue to be considered.
- Fin height is now the most influential parameter on heat transfer rate suggesting that an optimal value exists below 8.
- An increase in fin overlap results in minimal heat transfer rate increase at large pressure drop costs suggesting an optimal value has been passed an exists near 0.75.

Again these ME values are coupled with the overall heat transfer rate and pressure drop values in Figure 18 to create an encompassing picture of the DoE. As the parameters chosen had large influence on heat transfer rate, a common theme is observed in the DoE 2 data points: an increase in heat transfer rate is accompanied by a nearly equal increase in pressure drop and the target therefore still seems out of reach.

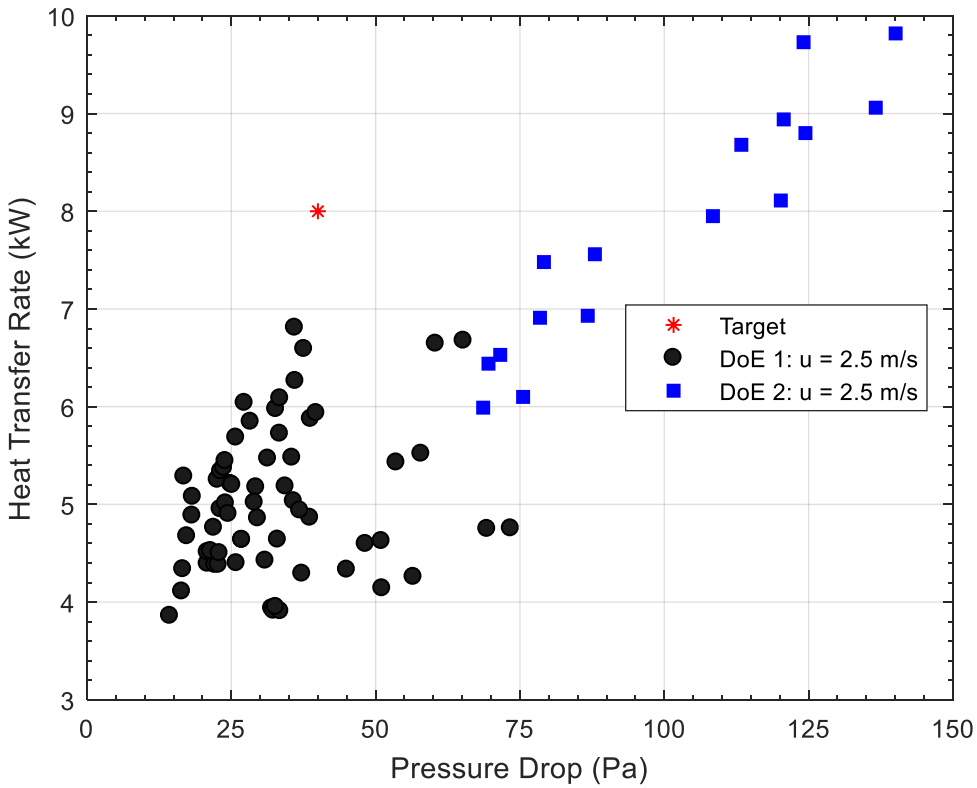

Figure 18: DoE 1 and DoE 2 heat transfer rate vs airside pressure drop results

At this point a foundation for responses to geometry changes exists and can be used to estimate where the optimal geometry combination may exist. Rather than continue performing DoE's and incrementally approaching the goal, UW's HPC cluster will be utilized to simulate large quantities of unique geometry combinations in approximately the right area and that stem from the main effects and raw values previously analyzed.

The basic process workflow of CAD modeling, generating a mesh, and simulating in Fluent remains the same for this analysis approach. Except the Fluent simulation is not conducted locally but rather a sent to the HPC cluster. This is beneficial for the sake of mass producing results quickly as the cluster utilizes many computers with superior hardware. The process of generating simulation journal files, shell scripting, and data extraction from the UW HPC system is outlined in great detail in Courtney

Leed's Master's Thesis[4]. For this work, a similar process is utilized but specific to the design problem on hand.

In addition to the influential parameters found in the previous two DoE's, a transverse Y and longitudinal Z offset are added to the investigation; Figure 14 outlined these two geometric features. Due to the nature of the tapered geometry, the majority of fin mass exists near the air channel base leaving the center of the air channel open. Airflow preferentially channels into these regions at the fin tips instead of near the fin base where larger flow rates are desired. The transverse and longitudinal offsets aim to remove this open area and force additional mixing of the fluid with minimal design change.

Table 6 shows the parameters used for this three-level DoE analysis and the performance results.

Table 6: DoE 3 setup and results

Parameter	Low	Mid	High	Pressure Drop (Pa)		Heat Transfer Rate (kW)	
				Main Effects	Normalized	Main Effects	Normalized
Eccentricity, E (-)	0.25	0.38	0.50	-6.56	-0.77	-0.56	-0.97
Fin height, H (-)	2.00	4.00	6.00	0.41	0.05	-0.17	-0.29
Fin overlap, C (-)	0.50	0.70	0.90	6.55	0.77	0.58	1.00
Transverse Pitch, ST (-)	1.50	1.75	2.00	-8.51	-1.00	-0.46	-0.79
Transverse Offset, Y(-)	0.00	1.00	2.00	-0.50	-0.06	-0.01	-0.02
Long. Offset, Z (-)	0.00	0.50	1.00	0.30	0.04	0.04	0.06

The following conclusions are made on each parameter:

- Base eccentricity results are consistent with what was previously found. While optimal values are low, due to manufacturing print head acceleration considerations and waterside cavity flow stagnation, selected values are limited to those in the table.
- Optimal fin heights have been significanlty reduced since the Baseline DoE and is no longer one of the most influential parameters, suggesting optimal values exist near the lower end of the

range. A tradeoff between an open airside and waterside cavity flow stagnation exists within this range and will be investigated in Waterside Convection Section 3.3.

- Fin overlap is again one of the most influential parameters and again yields similar takeaways: larger values increase surface-area to volume ratios but leads to an increase in pressure drop.
- Transverse pitch has similar takeaway to that of fin overlap. A smaller value leads to larger surface-area to volume ratios but also leads to larger pressure drop.
- Results for both the transverse Y and longitudinal Z offsets are mildly dissappointing. Adding these curvatures to the fin arrays seemling has little effect on overall performance. Appendix Sections 7.2.2 and show these two cases, one with and one without the offsets, and temperature contours visually exhibit a improved fluid mixing but the numbers suggest that the problem is simply convection to a bulk temperature and the mixing has little effect.

Figure 17 shows the heat transfer rate vs pressure drop results from this analysis relative to the results from the first two DoE's and the design target. The majority of the DoE 3 data points exist between DoE 1 and DoE 2 in a positive direction, suggesting that what was learned from the first two aided in properly setting bounds for the third. Numerous geometric combinations are oberverd hovering near the target design goal and the selected optimal geometry is highlighed having slightly greater heat transfer rate and slightly less pressure drop.

With a proposed airside geometry capable of performing at the target design goal, the next two sections cover details on the conduction and waterside-convection resistances used in the heat exchanger thermal model. Assumptions are clarified and considerations are made for compositie polymers and SS MIM materials.

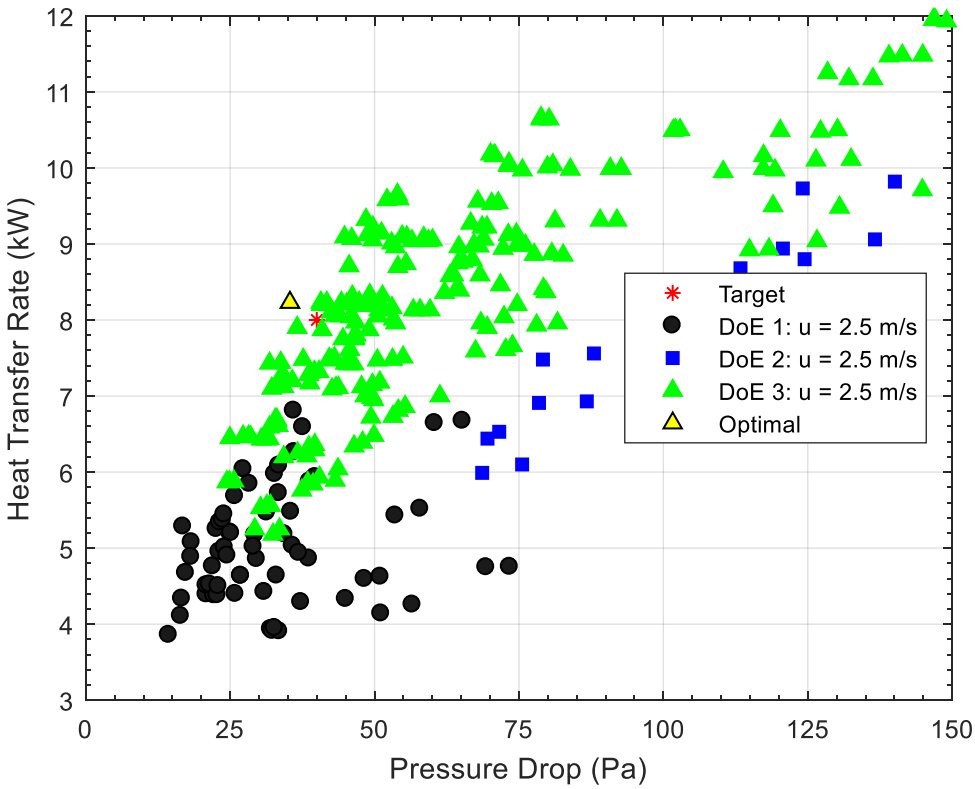

Figure 19: DoE 1, DoE 2 and DoE 3 heat transfer rate vs airside pressure drop results

3.2 Conduction

Conduction resistance in conventional HVAC heat exchangers is typically not the limiting factor, is relatively easy to calculate, and given by:

$$R_{cond} = \frac{th_w}{k_m A_c} \tag{12}$$

where th_w is wall thickness, k_m is material conductivity, and A_c is the cross-sectional area perpendicular to heat flow. In printed composite polymer heat exchangers, conduction resistance is more significant and complex due to low conductivities of the material, process induced anisotropic effects, and typically thicker walls to ensure water tightness.

Traditional neat-thermoplastic polymer thermal conductivities range from 0.1 – 0.3 W/m-K; however, to increase these conductivities fillers can be added to the base polymer. Common conductive fillers include copper, aluminum, graphite, carbon, etc. and come in an array of varying shapes: spheres, flakes, platelets, and fibers to name a few. Conductive fillers add implications to both the printability of the material and the effective thermal conductivity.

Flow-ability is a metric used to characterize how well a polymer matrix melt impregnated with a filler flows under printing conditions. As the volume percent of the filler increases, the flow-ability of the composite material decreases and thus there exists a limit to conductive filler content before the material is unprintable [2]. Two fillers investigated include short-strand carbon fibers and aluminum flakes. Figure 20 shows three Scanning Electron Microscope (SEM) images of such fillers: two of short-strand carbon fiber and one of aluminum flake fillers. As these fillers exist in the filament and flow with

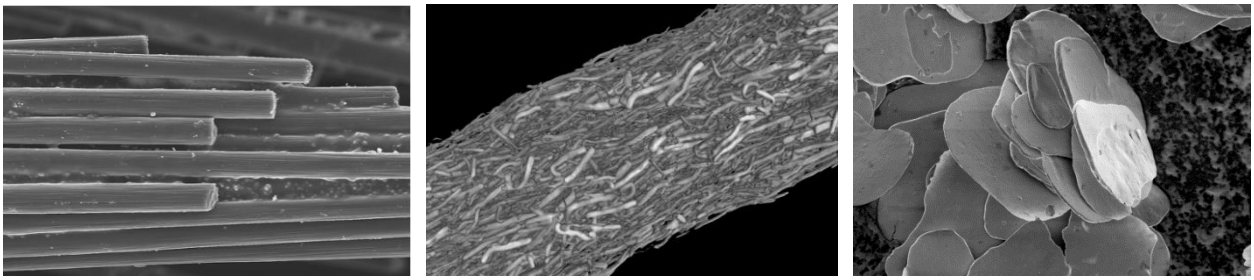

Figure 209: Polymer filler types: (Left) Carbon fiber (Middle) Printed nylon bead with short strand carbon fibers (Right) Aluminum flakes

the polymer melt through the nozzle, they preferentially orient with print direction. This process-dependent behavior and the spaghetti-like shape of the carbon fibers, results in the printed bead exhibiting high strength and high conductivity in the axial direction relative to the transverse directions. The aluminum flakes exhibit isotropic behavior in the only two directions associated with the printed bead plane and anisotropic behavior in the remaining out-of-plane direction. Figure 21 shows a simple example geometry to establish a nomenclature for anisotropic material properties. Thermal

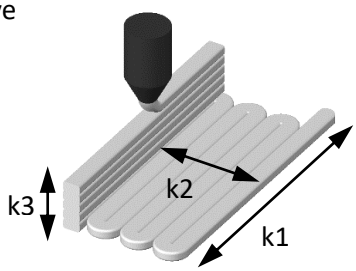

Figure 21: Anisotropic thermal conductivity nomenclature

conductivity in the print direction is k1, conductivity through adjacent bead lines in the x-y plane is k2, and conductivity through adjacent beads in the build or z-direction is k3.

Table 7 lists carbon fiber and aluminum flake (percent-by-volume) anisotropic conductivities values. The Markforged Onyx carbon fiber is a commercially available nylon based material and polycarbonate aluminum flake is a novel material developed for Thomas Mulholland's Ph.D. dissertation [2]. Conductivity k1 is typically largest followed by k2 and k3 as magnitude is dependent on overlapping or touching fillers to carry energy. These values along with other considerations help justify part print orientation to ensure the highest conductivities align with heat flow directions.

Table 7: Anisotropic thermal conductivities for various filled materials [2]

	k1 (W/m-K)	k2 (W/m-K)	k3 (W/m-K)
C.F. - Markforged Onyx	0.92	0.28	0.30
PC-AL Flake 7.5%	0.95*	0.95*	0.30*
PC-AL Flake 10.0%	1.75*	1.55*	0.32*

Reconsidering the optimized airfoil tool path with these conductivity values, Figure 22 shows how each of these filler types align with print direction and printed features. For the fibers, axial conductivity aligns with the fins and the lower transverse conductivity governs the conduction through the walls. For the flakes, the printed geometry exhibits nearly isotropic behavior in the x-y plane.

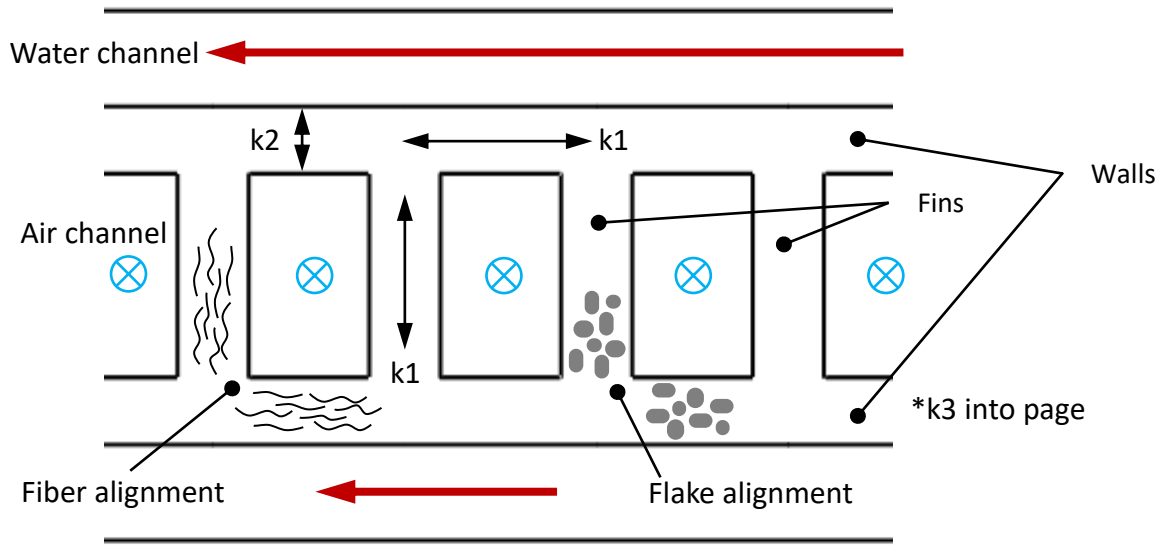

Figure 22: Fiber and flake filler content with process-dependent orientation as a results of the optimized airfoil microstructure tool path

Aside from the added strength fiber fillers yield, this preferential filler orientation poses an interesting thermal conductivity question on overall heat exchanger performance. Figure 23 shows heat exchanger heat transfer rate as a function of wall thickness at different assumed values of thermal conductivity: the first with the k1 and k2 values of 0.92 and 0.3 W/m-k respectfully, the second with isotropic values of 0.3 W/m-K, and the third with isotropic values of 0.92 W/m- K. At a fixed airside pressure drop and optimizing fin array DoFs at each wall thickness, the plot shows overall heat transfer rate of the anisotropic material hovering that of the lower k2 value. Meaning that at these conductivity values, overall performance is dominated by the k2 value than rather than the higher k1 value. The

return on using extended surfaces at these low conductivity values is minimal due to the process induced filler orientation and thus turning to a tapered geometry like introduced in the previous sections is further justified as conduction resistance is primarily limited by k2.

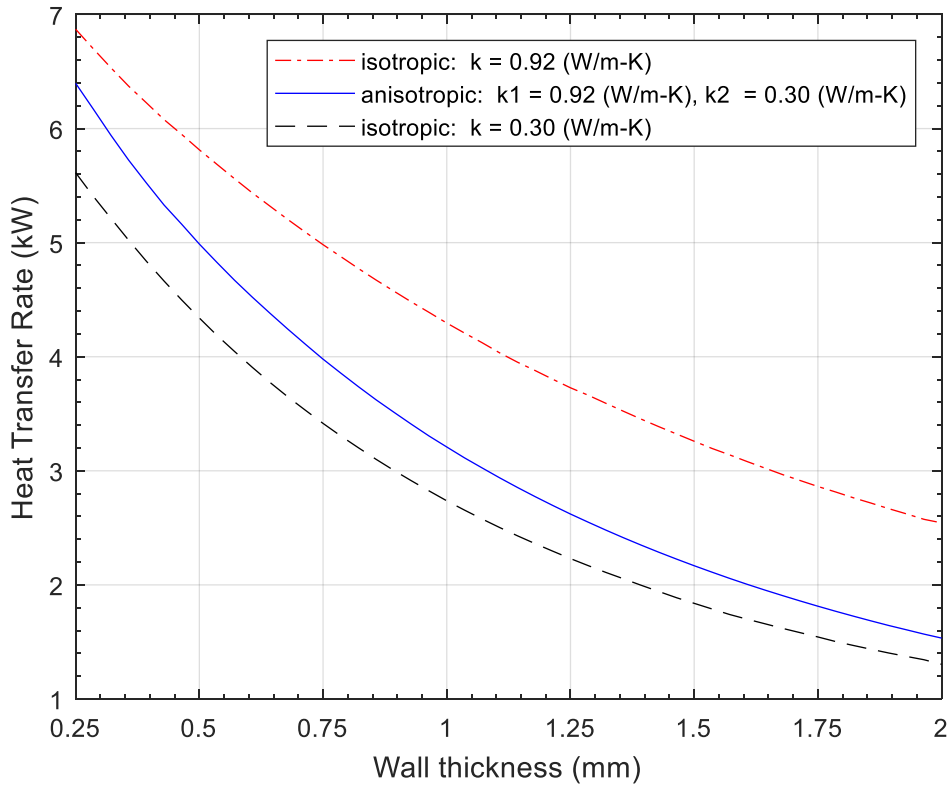

Figure 23: Airfoil heat transfer rate as a function of wall thickness at varying isotropic and anisotropic thermal conductivities all optimized for a 12" x 12" heat exchanger at constant airside pressure drop.

With the hollow tapered-pin fin geometry, Figure 24 shows optimized heat transfer rate as a function of thermal conductivity k2 with a fixed airside pressure drop. Observe a knee in the curve near 1 W/m-K and diminishing return on increasing conductivity after 2 W/m-K. At these conductivity values, airside convection resistance again becomes the largest limiting factor to overall performance. The assumption made here is that water flows within the hollow core of the fin and that no waterside thermal gradient exists. These assumptions are investigated and validated in Waterside Convection Section 3.3. Note that this optimization does not include the use of extended surfaces and that as conductivity approaches 10 W/m-K an optimal combination of hollow and extended surfaces could exist.

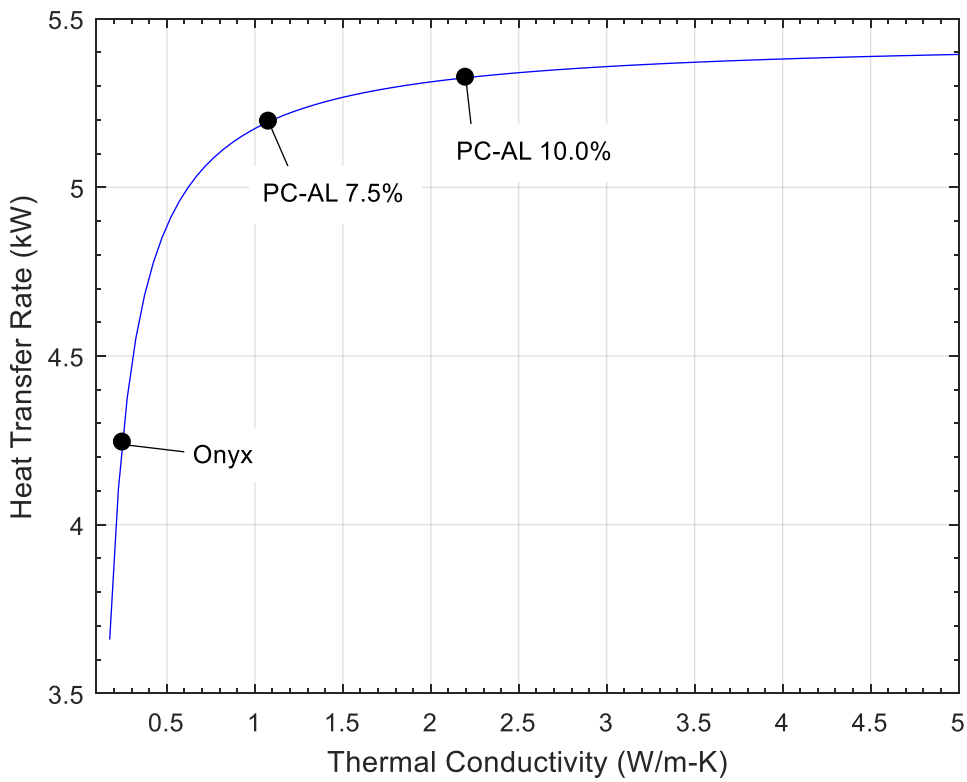

Figure24: Tapered-pin heat transfer rate as a function of thermal conductivity optimized for a 12" x 12" heat exchanger at constant airside pressure drop.

While a similar manufacturing process exists for printing 17-4 SS MIM materials, the post-sintering process results in a near fully dense part and k1, k2, and k3 thermal conductivities of 17, 17, and 13 W/m-K respectfully.

3.3 Waterside Convection

For more conventional geometries like the airfoil fin, standard duct flow correlations are used to calculate waterside heat transfer coefficients and friction factors. But for tool path, mass purposes, and conduction purposes, it is convenient to construct hollow airside finned features. On the waterside, this results in fin cavities that the water can enter and thus result in an overall shorter length of conduction. However, there exists the possibility of flow in the cavity to become stagnant as fin aspect ratio, height over base diameter, increases. Traditionally waterside thermal resistance is nearly negligible relative to others in the network but with hollow fins cores and potential stagnation regions, a further understanding of these features is needed. To investigate this behavior, the analysis considers the three scenarios shown in Figure 25 a straight duct with solid fins, a straight duct with waterside cavities, and a duct with waterside cavities and structure to persuade flow into the fin core.

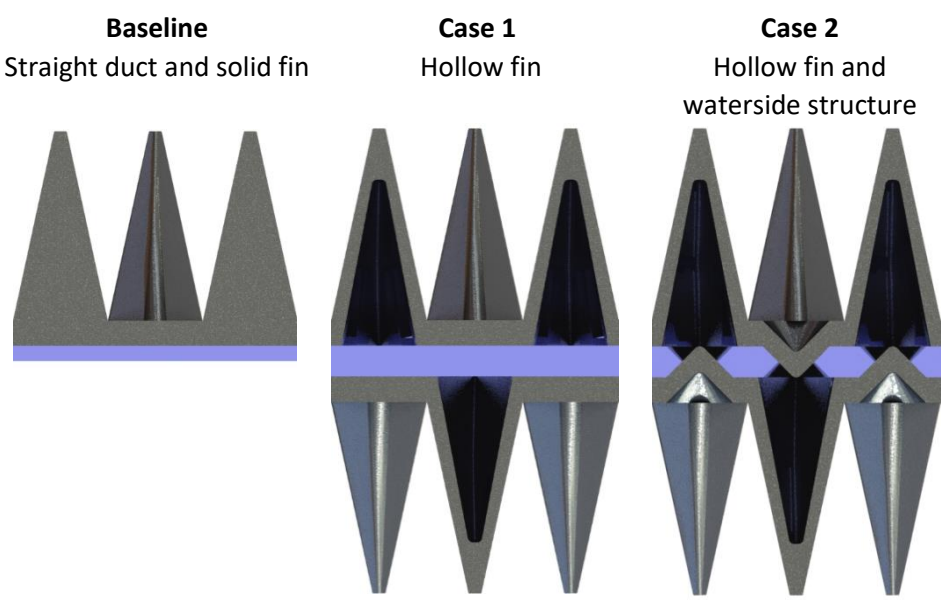

Figure 25: Waterside thermal and hydraulic case study setup

The first step in this analysis investigates the effect of removing all fin core material and assumes the worst case scenario of stagnant water within the cavity. The fin efficiencies for this scenario with materials having a thermal conductivity of 1 and 15 W/m-K are plotted against cavity depth in Figure 26. To achieve continuous tool pathing the dimensionless cavity depth must equal one and at this value fin efficiencies are observed to decrease by approximately ten percent.

Moving from the Baseline to Case 1 suggests a performance decrease but the fin efficiency analysis assumes purely stagnant flow. CFD simulations are utilized to validate this assumption. In each

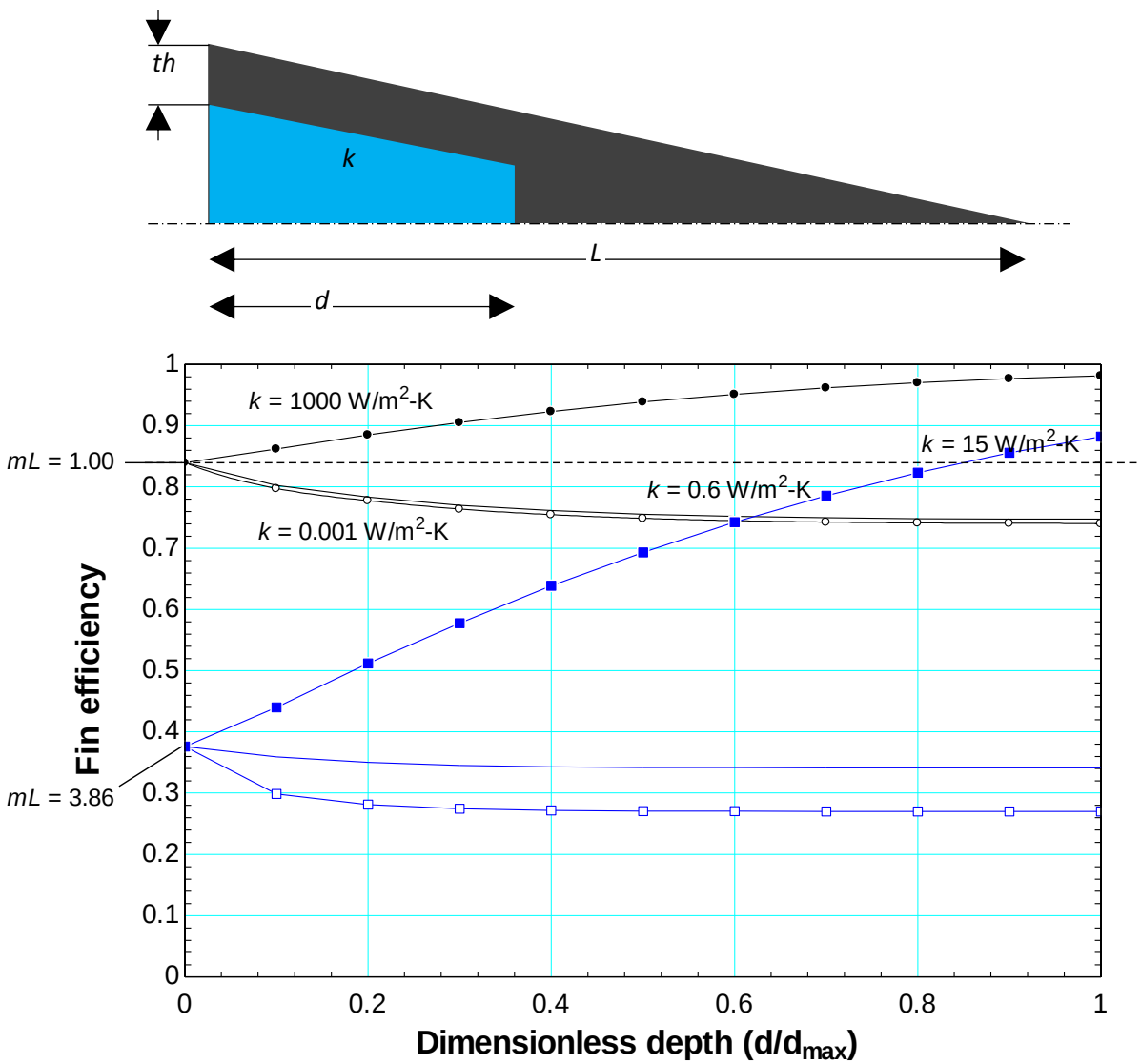

Figure 26: Fin efficiency as a function of waterside cavity depth at varying cavity thermal conductivities (analysis and figure credit: Mike Cheadle)

case, water inlet conditions and fin convection boundary conditions are set, and relevant parameters are extracted to compute the conductance and pressure drop. Table 8 shows the results from this CFD analysis.

Table 8: Waterside thermal and hydraulic results

	Baseline	Case 1	Case 2
UA (W/K)	0.30	0.31	0.34
ΔP/fin (Pa)	18.75	18.63	52.63
Normalized UA (-)	-	1.03	1.16
Normalized ΔP/fin (-)	-	0.99	2.81

Similar conductance and pressure drop is achieved in both the Baseline and Case 1. This is likely due to the cavities redeveloping boundary layers, generating higher overall heat transfer coefficients, and some fluid mixing near the fin base. As waterside structure is added to persuade flow into the base of the fin, a 16% increase in conductance and a 281% increase in pressure drop are observed. As suspected, the waterside fins aid in reducing stagnation regions but it comes at a price. However, this is the price to pay for opening up the airside and achieving the performance needed. With the proposed topology of the additive heat exchanger, overall waterside pressure drop is easily decreased by even the slightest increase in water duct height.

Again, rather than perform comprehensive design studies on all combinations of waterside bump height, channel height, fin eccentricity, fin height, etc., the conclusion is made that adding a waterside bump significantly persuades flow into the fin cavity eliminating detrimental waterside thermal gradients. Fins with low eccentricity values are ideal from an airside streamlining perspective but result in a narrow waterside cavity and fins with low height values are ideal as the result in an overall shorter cavity. To visualize these effects, Figure 27 shows three geometric scenarios with fixed E at three different H values. In each scenario, velocity vectors are overlain a waterside temperature

contour to illustrate to the water circulation into the fin cavity and the waterside temperature gradients. As H increases from 2 to 6, the fin tip temperature decreases as water circulation effectiveness also decreases. From an airside perspective, larger H values are ideal to open up the geometry for lower pressure drops but on the waterside, a limit exists to maintain thermal effectiveness. The pros and cons of this behavior is weighed against the airside convection analysis to properly set bounds on geometric relations in a full-scale heat exchanger model.

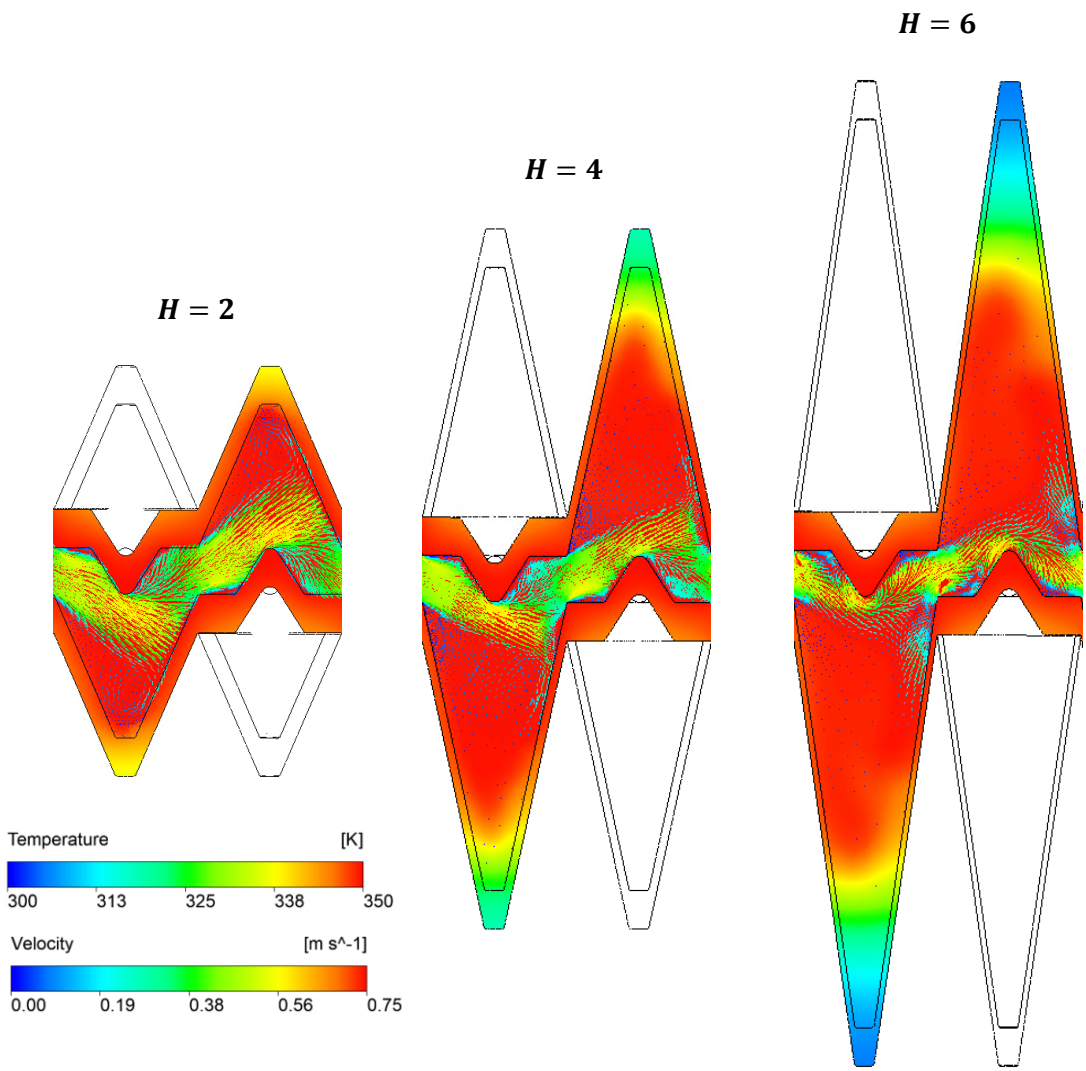

Figure 27: Waterside thermal gradient visualization with constant E at various values of H

At the full-scale heat exchanger level, inlet and outlet headers locations are justified to achieve proper flow distribution in each channel and for practicality of having each on the same side of the component. CFD model velocity contours for a full-scale heat exchanger with straight ductwork are shown in Figure 28. Measuring the mass flow rate in each channel at Section A yields 5.4% flow mal-distribution from the average. At the effectiveness ranges typical for HVAC application, ~0.50, this deviation from the average in each channel is considered acceptable. While a full scale heat exchange model to include the cavities and waterside structure is desired, too much computational power is needed to accurately capture all aspects of its behavior. However, as previously discussed the waterside structure increases total pressure drop per fin nearly two-and-a-half times and with this increased pressure drop becomes better flow distribution; by nature of water wanting to follow the path of least resistance. Appendix Section 7.3.5 outlines model and experimental data for a full-scale waterside-duct pressure-drop analysis.

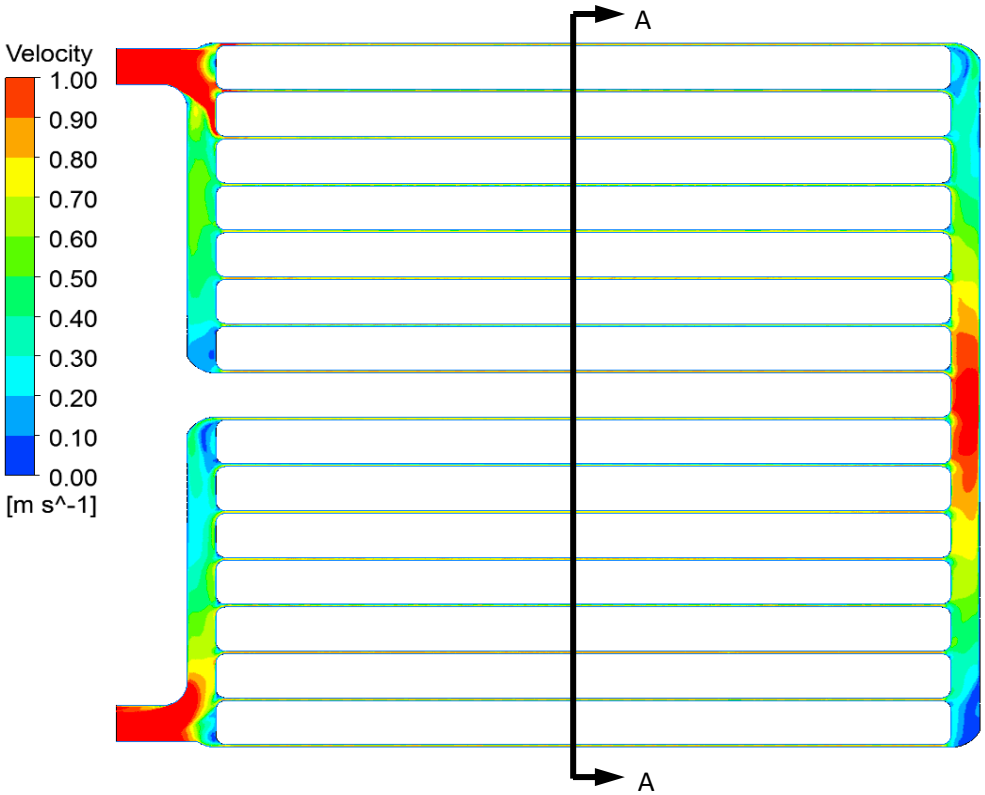

Figure 28: Full-scale HX waterside flow distribution and pressure drop CFD

3.4 Thermal Modeling Conclusions

After understanding the thermal resistance network and form drag concepts, numerical methods are utilized to optimize overall heat exchanger thermal and hydraulic performance. The thermal resistance network from Figure 9: Heat exchanger thermal resistance networks for solid and hollow fin types. 9 and the $\varepsilon - NTU$ method characterize heat transfer rate and equation 2 characterizes total pressure drop. With performance dependent on the geometry and material properties, maximum heat transfer rate is desired for given flow conditions and pressure drop. Figure 29 shows the optimal heat transfer rate for various geometries and materials at equivalent airside-pressure-drop. Two relationships are observed, one with geometry and one with material. The hollow-tapered geometries outperform the extended surface airfoil geometry due to the overall shorter length of conduction. The tapered ellipse geometry outperforms the tapered pin and airfoil geometries as it combines the short conduction path with an open and streamlined airside. And as material conductivity increases, so does heat transfer rate.

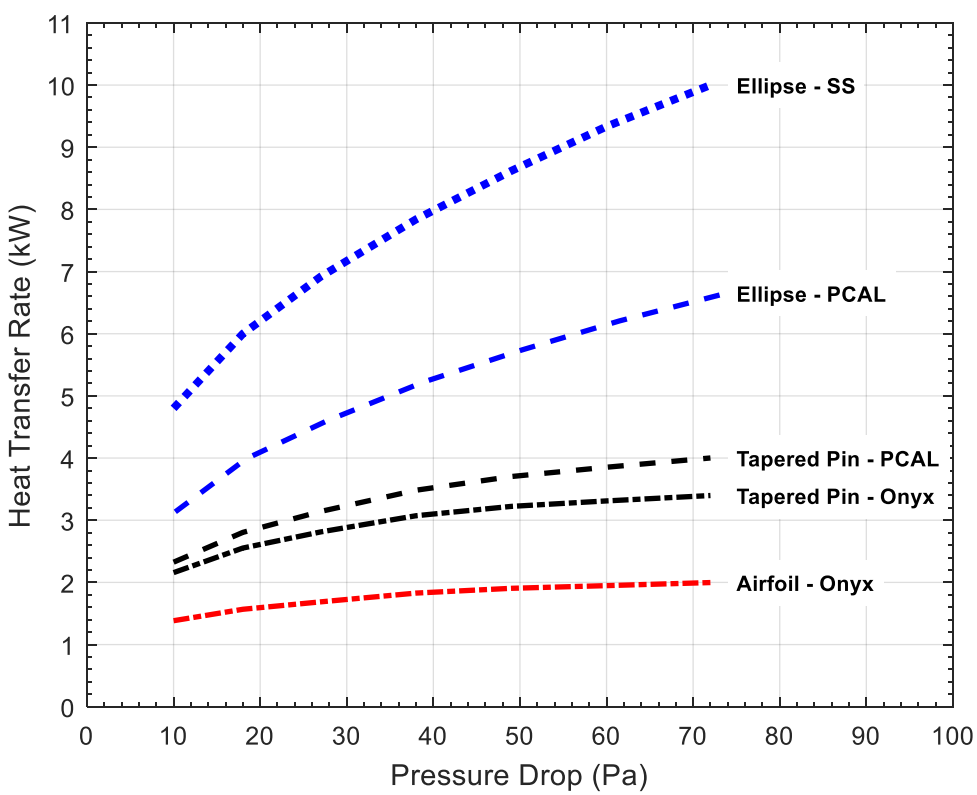

Figure 29: Optimal heat transfer rate for various geometry and material combinations at a fixed airside pressure drop

Along with heat transfer rate $\dot{q}$ a few other metrics that are used to quantify and compare performance metrics are the airside heat transfer coefficient $\dot{h}$, the airside surface-area to volume ratio $\frac{m^2}{m^3}$, and the heat exchanger mass to volume ratio $\frac{kg}{m3}$. At a constant $40\ Pa$ airside pressure drop, these metrics are outlined in Figure 30: Heat exchanger heat transfer rate and average heat-transfer-coefficient for different geometry types and materials at face velocity u_f of $2.5\frac{m}{s}$ and airside ΔP_a of $40\ Pa$.Figure 30 and Figure 31.

Figure 30 shows heat transfer rate and average airside heat transfer coefficient for various geometries and material combinations and two conclusions can be made. First, as material conductivity increases, heat transfer rate increases for each geometry type. Second, a larger heat transfer coefficient is not correlated to a larger heat transfer rate. The tapered pin geometry yields the largest heat transfer coefficient due to the on-average smaller feature sizes but heat transfer rate suffers because the

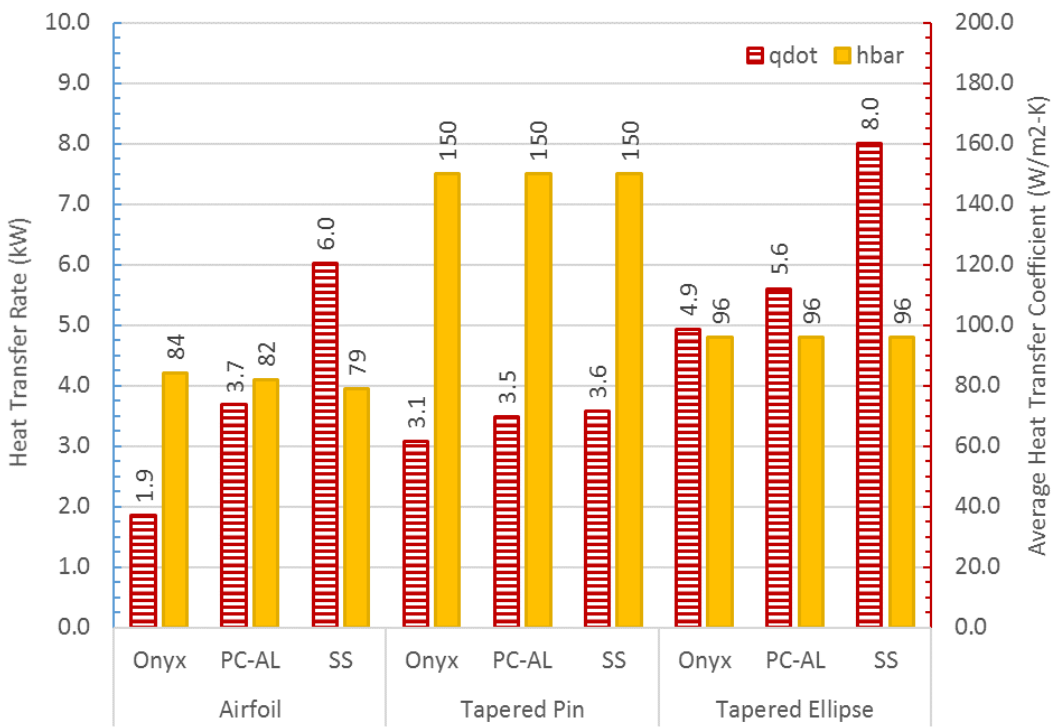

Figure 30: Heat exchanger heat transfer rate and average heat-transfer-coefficient for different geometry types and materials at face velocity u_f of $2.5\frac{m}{s}$ and airside ΔP_a of $40\ Pa$.

geometry is paying a large price to form drag. Since there is a larger form drag or pressure drop per fin, fewer fins consume the allotted airside pressure drop resulting in less surface area and a greater airside thermal resistance to heat transfer. Again, a push-pull relationship is observed between the heat transfer coefficient and pressure drop. The airfoil and tapered ellipse geometries have significantly smaller heat transfer coefficients but yield higher heat transfer rates as both are streamlined with the latter also having shorter conduction path lengths.

Figure 31 shows airside surface-area to volume ratio and the heat exchanger mass to volume ratio and two conclusions can be made. First, an inverse relationship exists with the heat transfer coefficient and the surface-area to volume ratio. As the heat transfer coefficient increases, the ratio decreases. Second, polymer heat exchangers are less heavy than steel heat exchangers but the hollow geometries are significantly less heavy than the solid airfoil geometry. More mass leads to larger material costs and

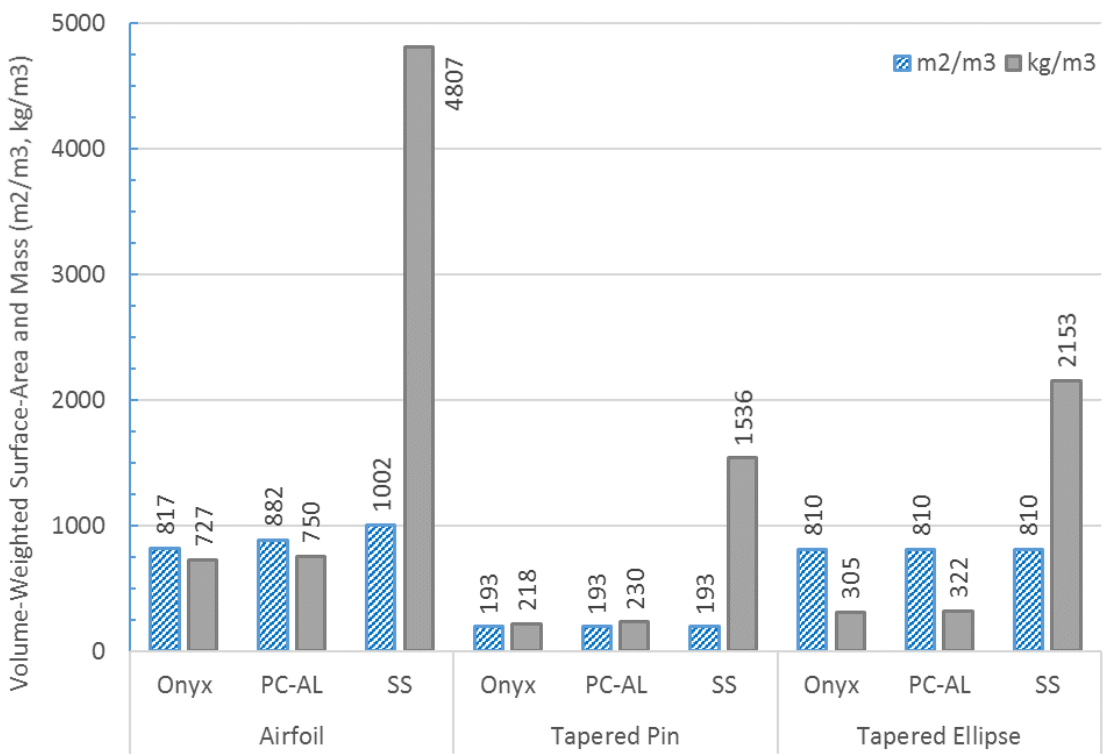

Figure 31: Heat exchanger volume-weighted surface-area and volume for different geometry types and materials at face velocity u_f of $2.5\frac{m}{s}$ and airside ΔP_a of $40\ Pa$.

longer manufacturing times.

4 Experimental Validation

The experimental setup used to validate heat exchanger performance is a modeled after the ASHRAE Standard 33 for testing air-cooling and heating coils. All necessary measurements to obtain heat transfer rates and pressure drops for both working fluids have been instrumented. On the airside, these measurements include inlet temperature, outlet temperature, pressure differential across the heat exchanger, and pressure differential across a nozzle in the duct; the nozzle pressure differential is used to calculate air mass flow rate. On the waterside, these measurements include inlet temperature, outlet temperature, pressure differential across the heat exchanger, and a mass flow measurement. The setup accommodates a heat exchanger with a 2.75" by 2.75" area. At this size, the test loop is kept small and inexpensive while maintaining the capability to validate the full-scale models. Details on the test loop and instrument specifications can be found in Appendix Section 7.3.

Using approximate operating temperatures and flow rates scaled from the full heat exchanger, the test-section duct-velocity is varied and all necessary measurements are taken to characterize the energy transfer for both fluids. Test results from the optimized airfoil geometry with the Onyx material are shown in Figure 32. The figure demonstrates the agreement of energy transfer measurements between airside and waterside fluids along with the thermal model used to determine the geometries. There is significantly less uncertainty in the waterside measurement than the airside due to the means of how mass flow rate is measured for each flow. For waterside mass-flow, a Coriolis flow meter is used and for the airside, pressure drop through a nozzle is used per ASHRAE Standard 41.2.

The tapered-pin fin thermal model is validated with waterside test results for a single geometry with three different materials in Figure 33. The three materials used are neat-nylon, Onyx, and PC-AL 7.5% with k2 conductivities of 0.20, 0.28, and 1.06 W/m-K respectfully. These results validate the process-dependency observed when printing with different filler types as the geometry in each case remains constant.

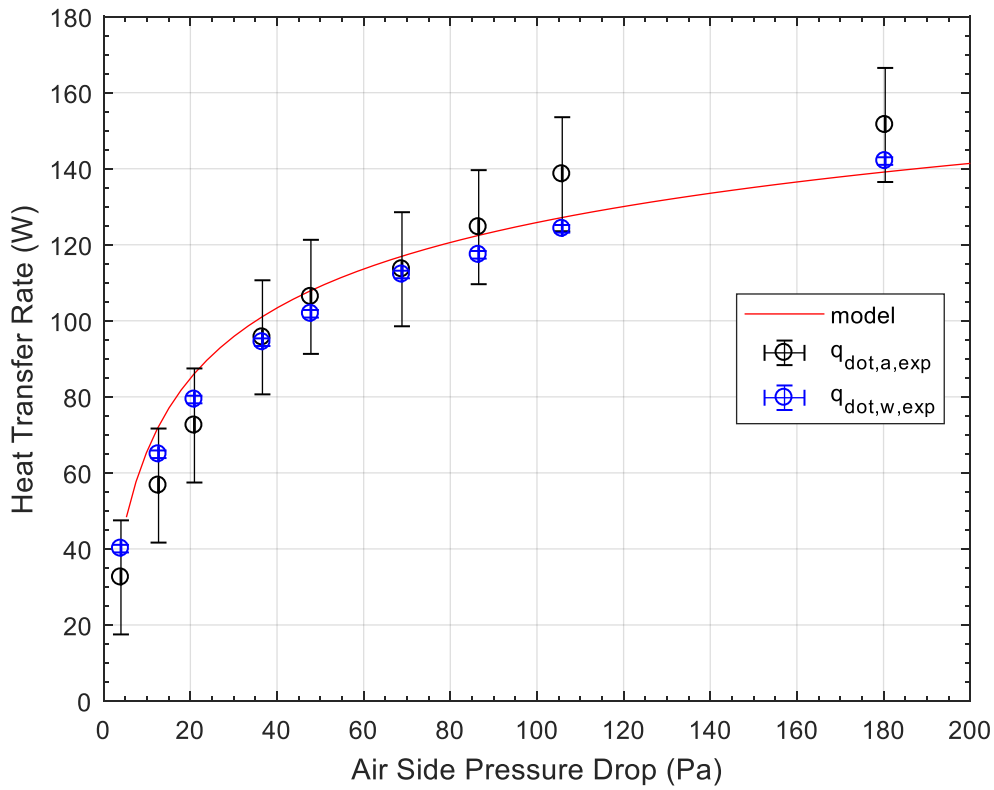

Figure 32: Airfoil - Onyx air and waterside heat transfer rate data vs airside pressure drop data comparison to thermal model

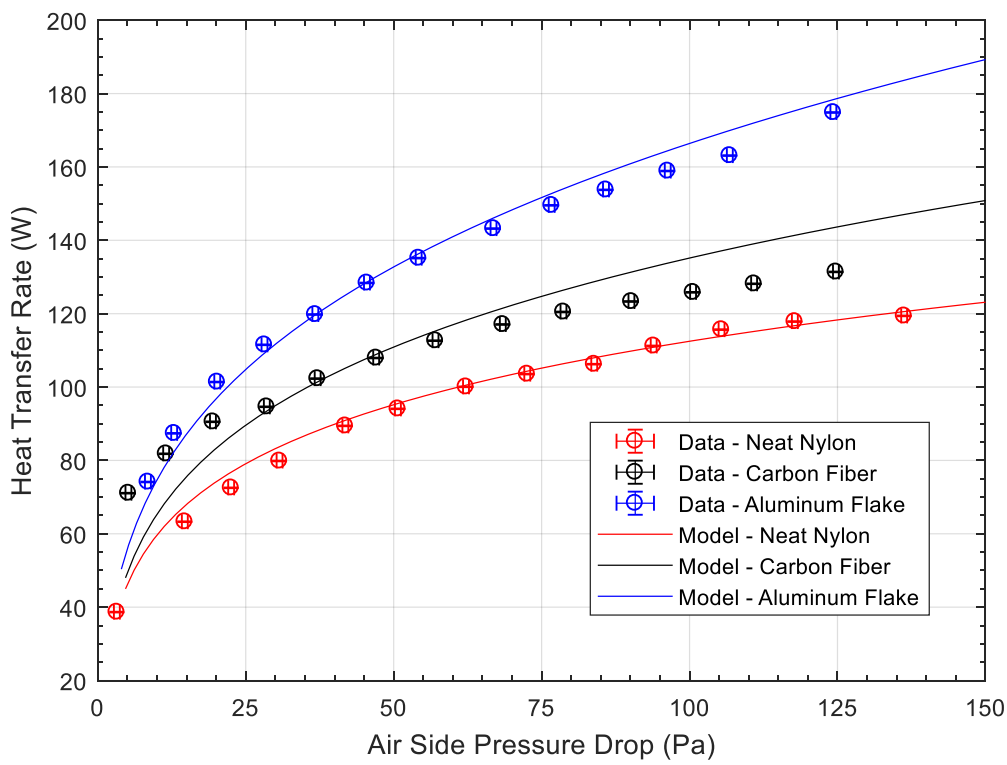

Figure 33: Tapered-pin fin test results and models for three heat exchangers printed with three different materials.

While the end-goal 17-4 SS MIM deposition process being developed in parallel, an EOS M290 DMLS machine at the University of Wisconsin's Grainger Institute is utilized to validate the tapered ellipse and stainless steel modeling as the deposition process becomes ready for prime time. To validate both airside and hollow-waterside modeling efforts, three cases are considered.

- Baseline: a solid airside fin with optimal geometry selected after DoE 2
- Case 1: the same airside geometry as in the baseline case with a hollowed fin
- Case 2: the optimal DoE 3 geometry with hollow fins with waterside structure to persuade flow into the fin cavity.

Figure 34 shows the as-printed heat exchanger for each case.

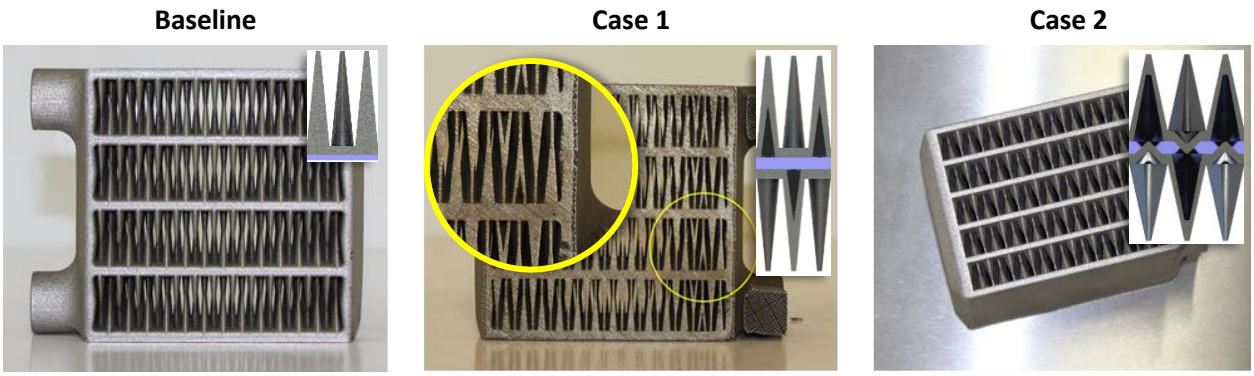

Figure 34: Tapered ellipse as-printed heat exchangers

In all cases, each geometry is designed to be manufactured using the deposition process with wall thickness dependent on extrusion nozzle diameter. The purpose of manufacturing with a DMLS machine is to validate the modeling as the deposition process is developed in parallel and lags this work. Scaled test results for these three cases are presented in Figure 35 and show agreement to the thermal models. Per the waterside CFD study, the baseline case and case 1 are observed to have very similar performance. Optimizing the geometry in case 3 and adding the waterside structure results in an overall

increase in heat transfer rate for similar pressure drop. The Case 2 geometry hits the 8 kW heat transfer rate at 40 Pa pressure drop design requirement.

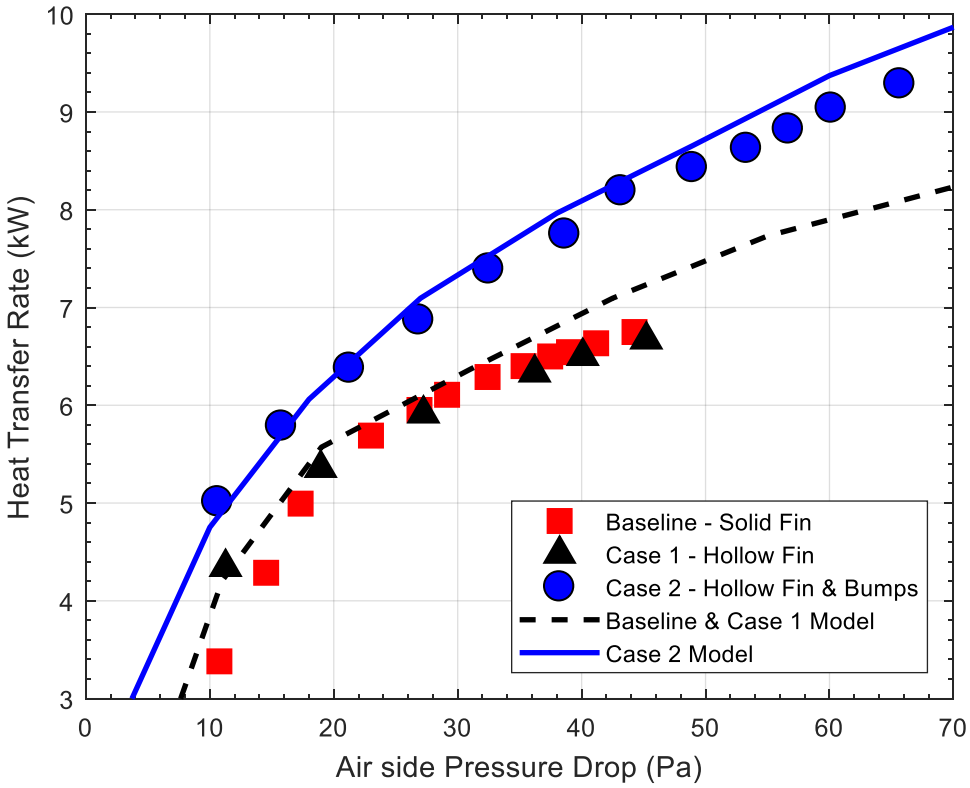

Figure 35: Tapered ellipse experimental test data and models for all three different waterside cavity cases

For all test-data and model comparisons presented, agreement between the thermal models and data part as pressure drop increases. An increased pressure drop corresponds to a larger face velocity and thus a higher Reynolds number flow. As briefly touched upon before with additively manufactured parts, the resultant surface is not rough but rather bumpy due to process-dependent effects like layer height and nozzle diameter. Fortunately, at low Reynolds numbers, assuming smooth surfaces for modeling simplicity is appropriate as standard HVAC heat exchangers operate in this regime. However, if desired operating conditions were to extend into the turbulent regime things might change.

5 Conclusions

In this work, concepts to address traditional limiting factors and additive-manufacturing challenges in air-cooled heat exchangers were developed. Continuous tool path first-principles were established for manufacturing heat exchanger geometries capable of operating at temperature and pressure. This concept and the use of low-thermal-conductivity materials pivoted geometry development from convectional extended surface geometries like the airfoil to the tapered and hollow geometries presented. The hollow geometries enable continuous tool pathing but also allow for overall shorter conduction path lengths while opening up the airside geometry to lower static pressure drops. The proposed stainless-steel hollow-tapered ellipse with waterside structure to persuade flow into the fin cavities takes advantage of all the described attributes making for an efficient use of material mass and arriving at a heat exchanger geometry capable of performing at and above HVAC standard coils. While the PCAL composite-polymer is less competitive than the stainless steel, the geometry still poses competitive numbers for specialty heat exchanger applications where additional corrosion resistance or lightweight components are required.

Having identified deposition additive manufacturing constraints and arriving at the tapered ellipse geometry, next steps include cycle testing and lifetime validation. Little is known about how thermal-pressure cycling effects on weld strength between layers and this investigation could yield interesting conclusions on the technology. Additional next steps may also involve continued work on geometry development. While additive manufacturing technologies and materials continue to be developed, the unparalleled freedom in design for heat exchanger geometries will continue to be an interesting design problem for the creative engineer.

6 References

[1] G.F Nellis and S.A. Klein. (2009) *Heat Transfer.* New York: Cambridge University Press.

[2] T. Mulholland. (2018) *Additive Manufacturing of a Polymer Composite Heat Exchanger.* University of Wisconsin – Madison Ph.D. Dissertation.

[3] R. Felber. (2017) *Simulation, and Testing of Novel-Air Cooled Heat Exchangers Manufactured by Fused Filament Fabrication.* University of Wisconsin – Madison Master's Thesis.

[4] C. Leeds. (2018) *Simulation of Tapered-Pin Fins and Cylinders in Crossflow.* University of Wisconsin – Madison Master's Thesis

[5] C. Wright (2018) *Analysis of Microstructure in a 3d Printed Heat Exchanger.* University of Wisconsin – Madison Master's Thesis

7 Appendix

7.1 Additive

7.1.1 3D Printers

Figure 36: 3D printers used in this project. (Left) Makergear M2 (Middle) Makergear M2 heated enclosure (Right) EOS M 290.

7.1.2 Printed Heat Exchangers

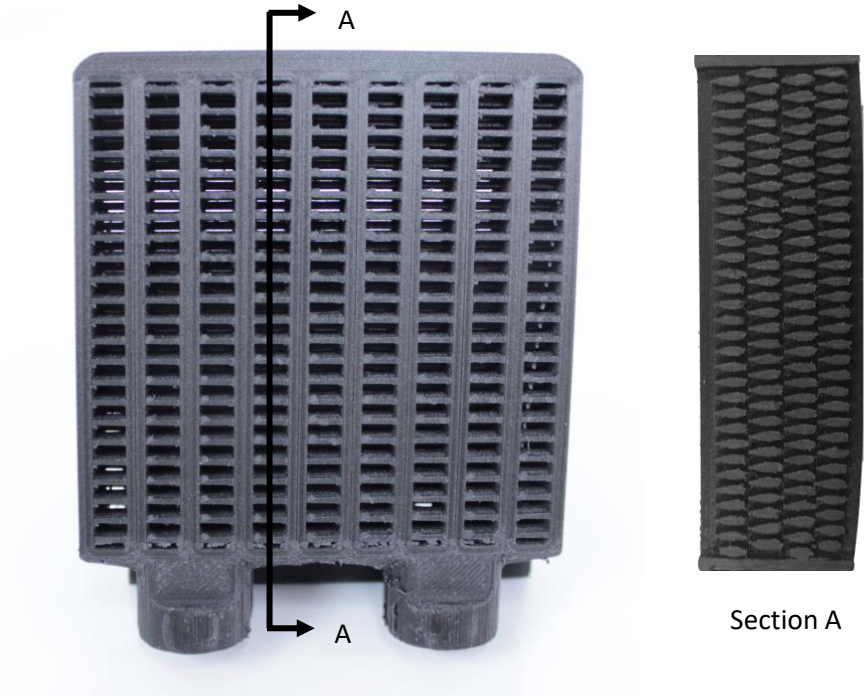

Figure 37: As-printed airfoil-onyx heat exchanger. Frontal area ~2.75" by 2.75"

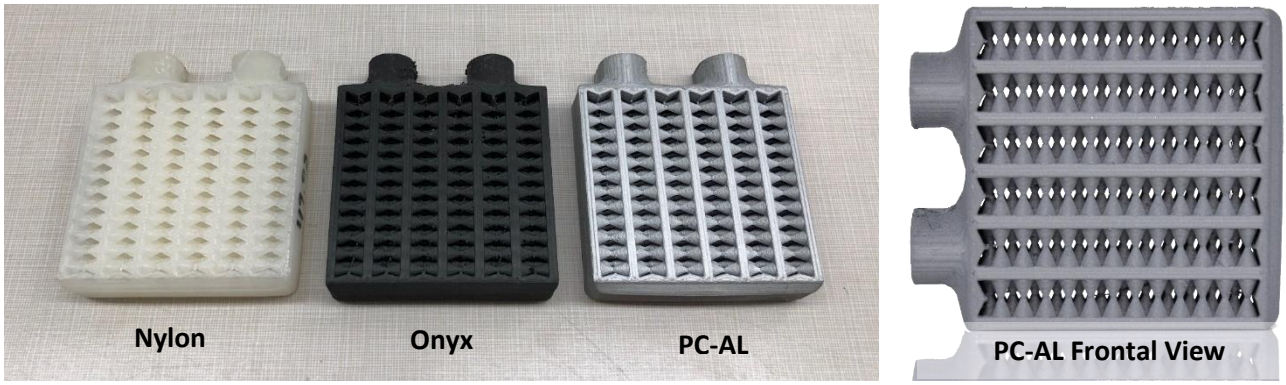

Figure 38: As-printed tapered-pin heat exchangers for various materials

Graveyard of printed heat exchangers

Figure 39: Printed heat exchanger graveyard

7.2 Thermal

7.2.1 Microstructure CAD Drawings

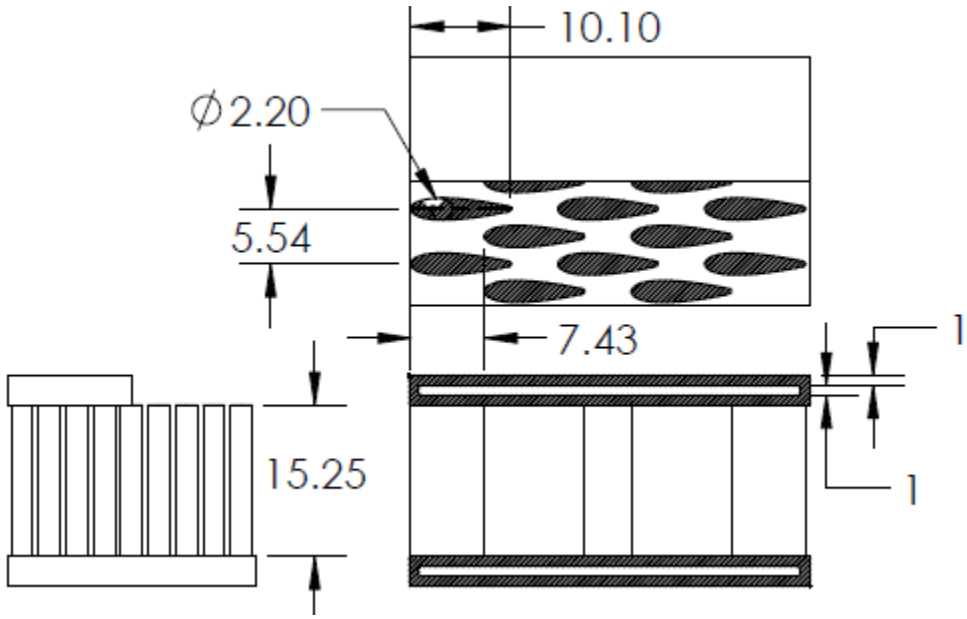

Figure 40: Airfoil microstructure CAD drawing

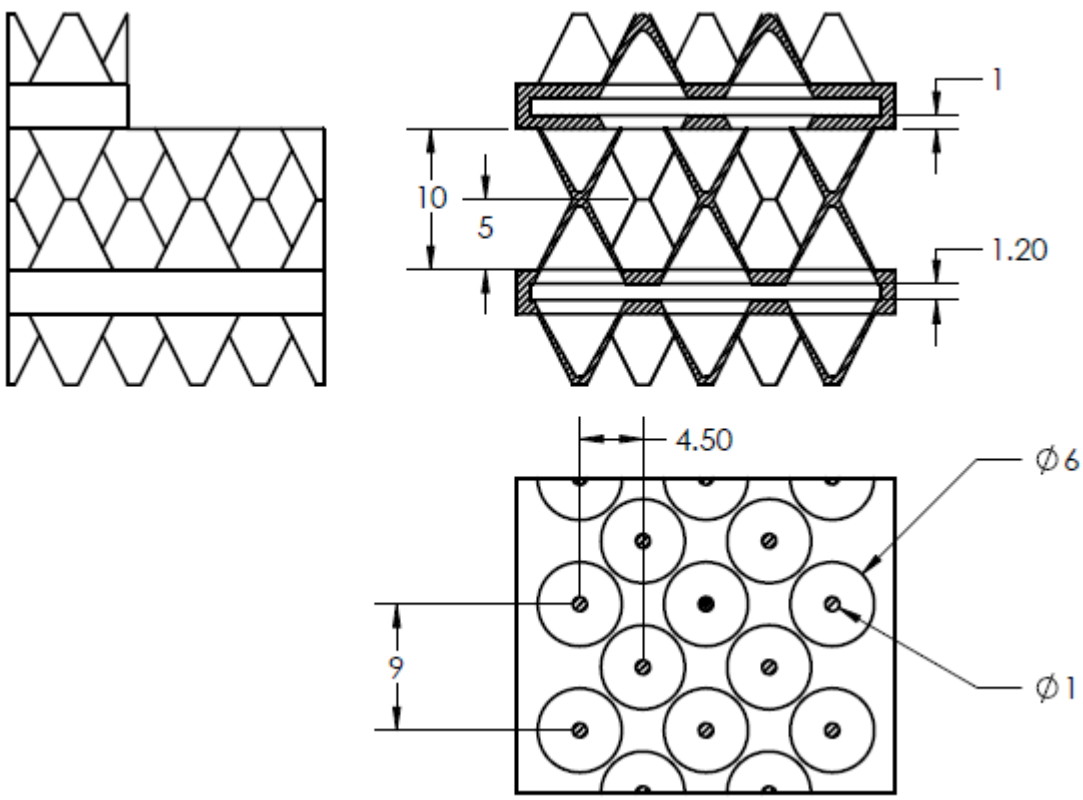

Figure 41: Tapered-pin fin microstructure CAD drawing

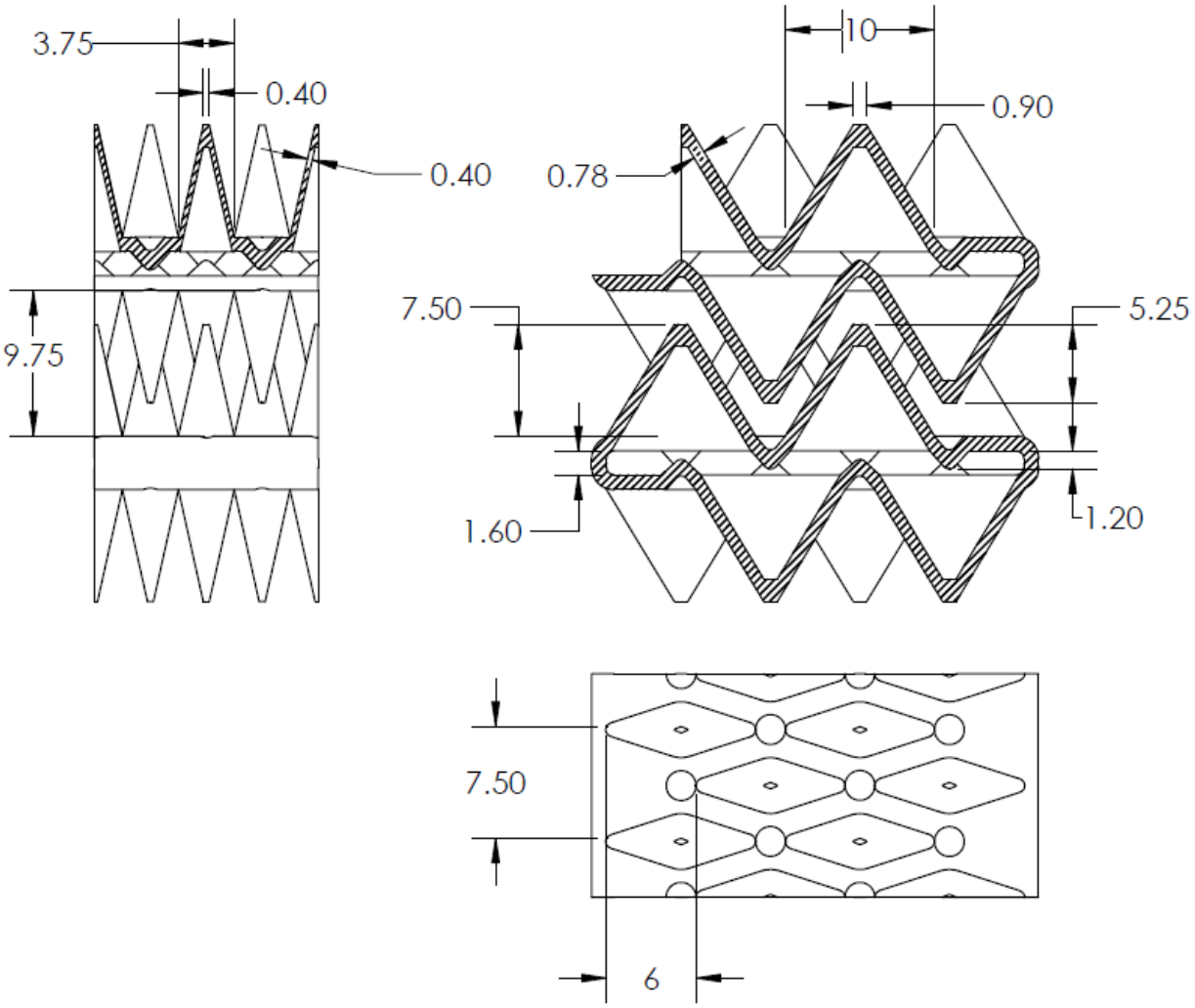

Figure 42: Tapered ellipse microstructure CAD drawing

7.2.2 Temperature Contours

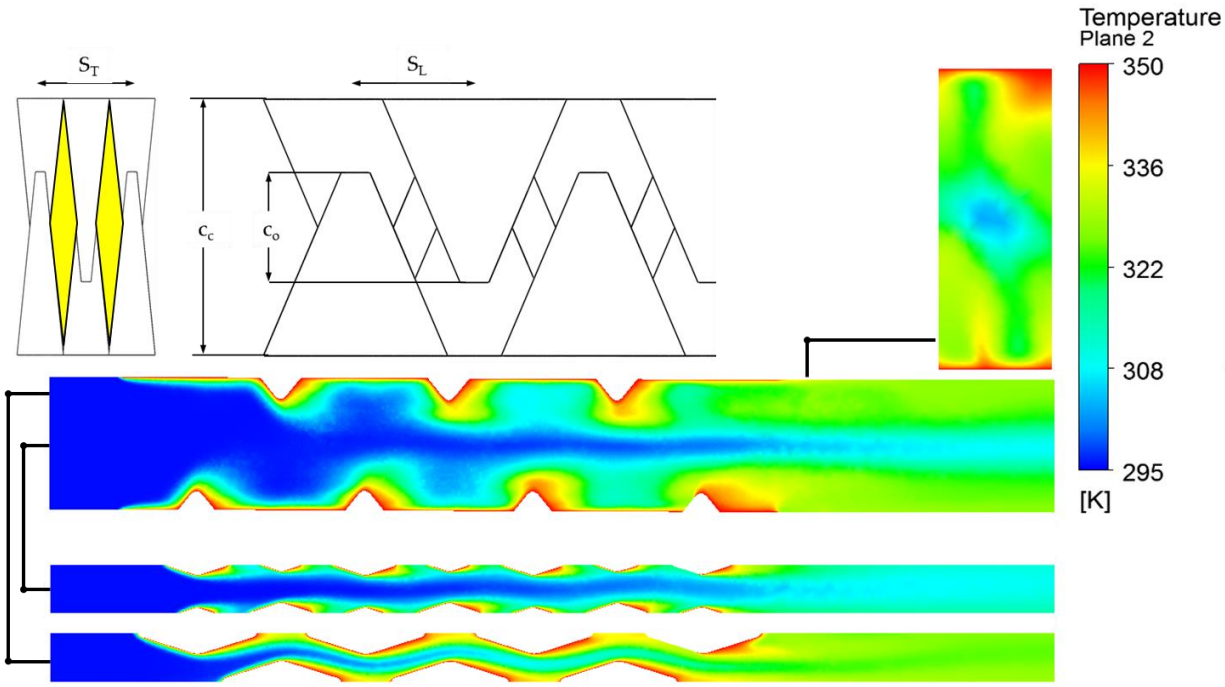

Figure 43: Temperature contours of computational unit cell for Y =0 and Z =0

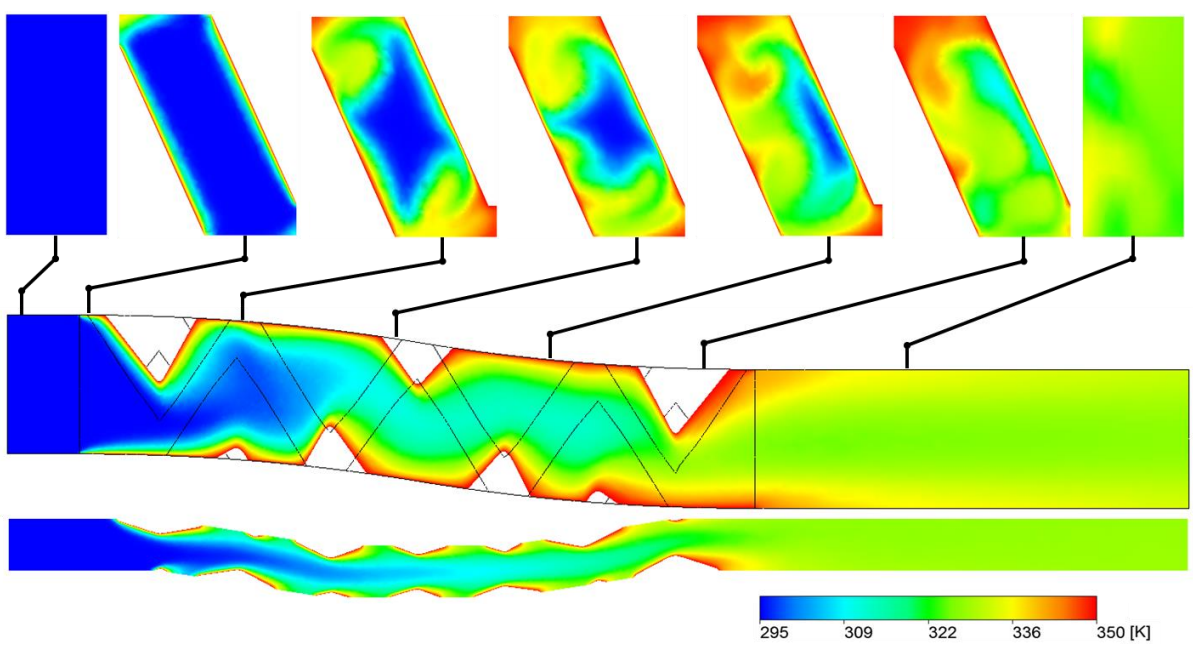

Figure 44: Temperature contours of computational unit cell for Y = 2 and Z = 1

7.3 Experimental

7.3.1 Test Loop Instrument Schematic

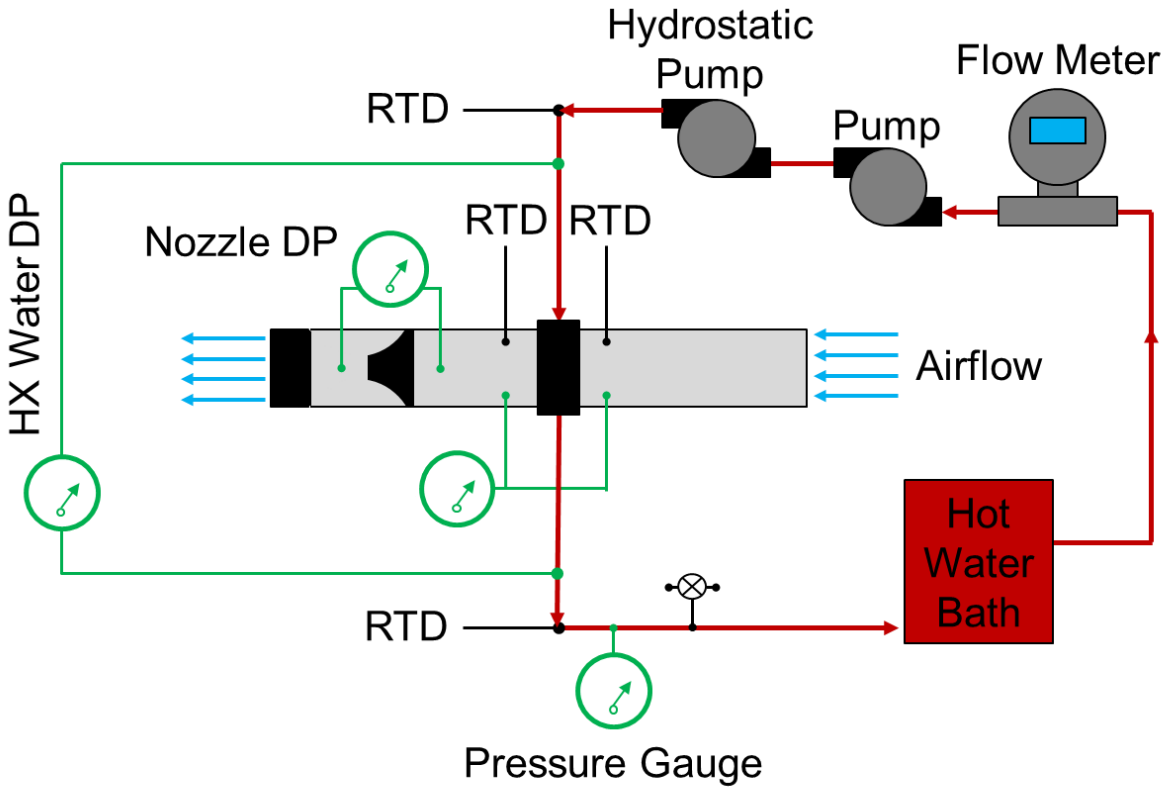

Figure 45: Test loop instrument schematic

7.3.2 Test Loop Instrument Specifications

Table 9: Test loop instrument specifications

	Component	Description
Waterside	Water Bath	NESLAB RTE-111
		Temperature Range: -25°C to +100°C
	Flow meter	Coriolis flow meter
	Pump	Micropump GJ Series
		Maximum ΔP: 55 psi
	Hydrostatic pump	Wheeler-Rex 29200
		Maximum Pressure: 250 psi
	RTD	Omega Ultra Precise RTD Sensor
		P-M-1/10-1/8-6-0-P-3 (closed end)
		Pt100 (100Ω at 0°C, 0.00385Ω/Ω/°C)
	HX Pressure Differential	Omega Px2300-10DI
		Pressure Range: 0-10 psi
		Accuracy: 0.25%
Airside	Blower	San Ace B97
		Airflow: 47.3 CFM
		Static Pressure: 3.052 inH2O
	RTD	Omega Ultra Precise RTD Sensor
		P-L-1/10-1/8-6-0-P-3 (open end)
		RMSD Accuracy: 0.03°C
	HX Pressure Differential	Siemens 7MF4432-1BA22-INC1Z
		Pressure Range: 1 to 2000 Pa
		Accuracy: ±0.5 Pa (resolution)
	Nozzle Pressure Differential	Dwyer MS-111 Magnesense
		Pressure Range: +/- 1 psi
		Accuracy: +/- 1%

7.3.3 Test Loop Image

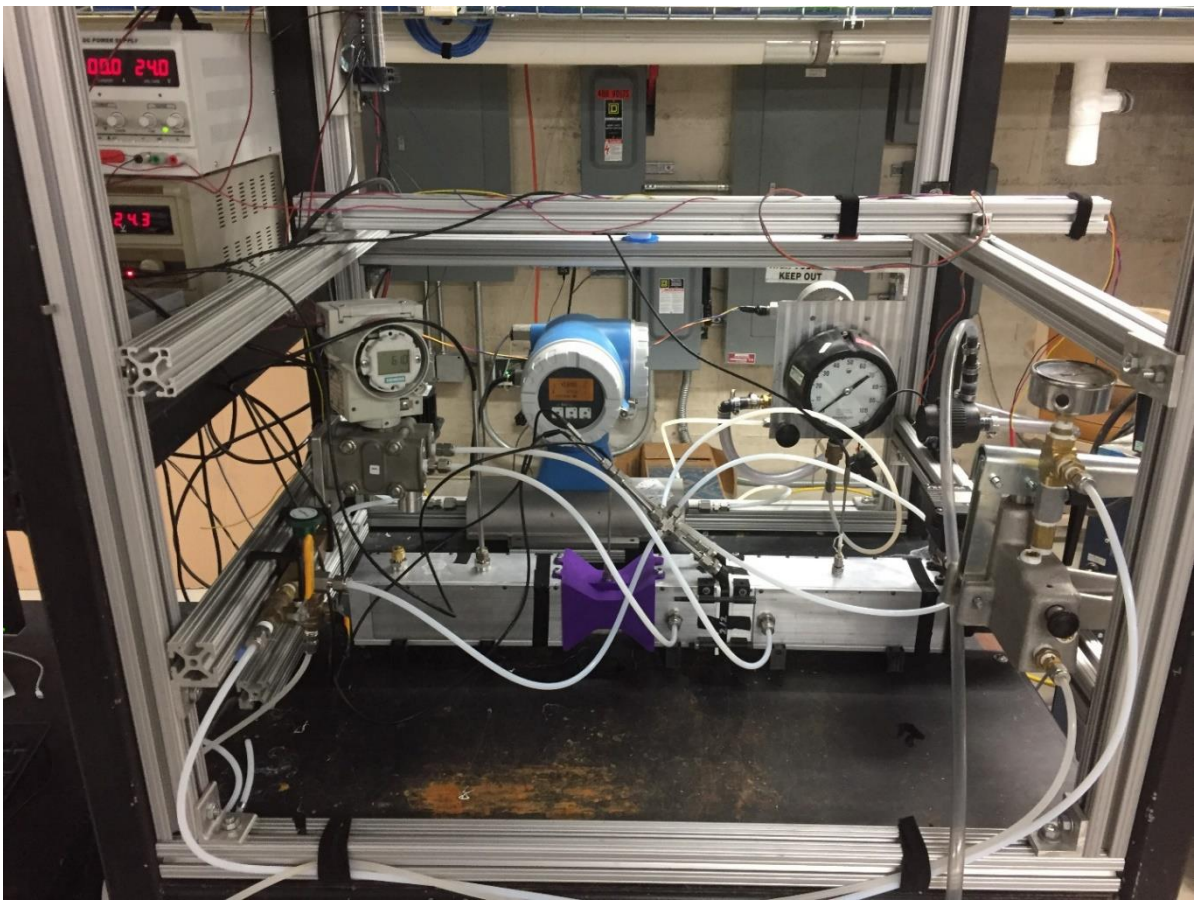

Figure 46: Image of test facility

7.3.4 Kazoo Pressurization

7.3.4.1 DoE

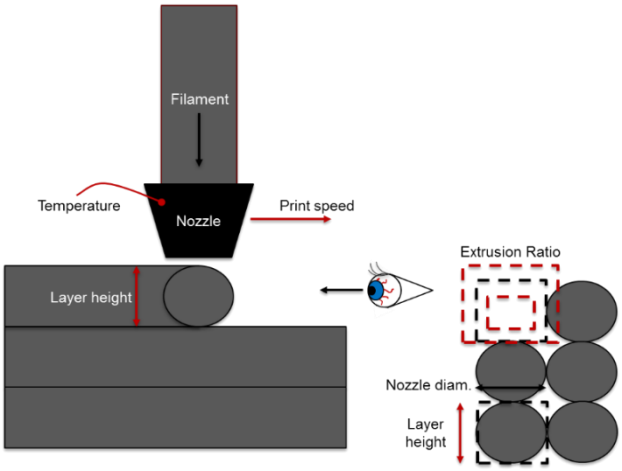

Table 10: Kazoo Pressurization DoE Setup and Results

Parameters	Low	High	Burst Pressure (psi)	
			Main effects	Normalized
Max per. Speed (S)	30	40	-15.6	0.70
Nozzle temp (T)	280	300	5.1	-0.23
Extrusion ratio (E)	1.05	1.1	13.5	-0.60
Layer height (H)	0.1	0.2	-22.4	1.00

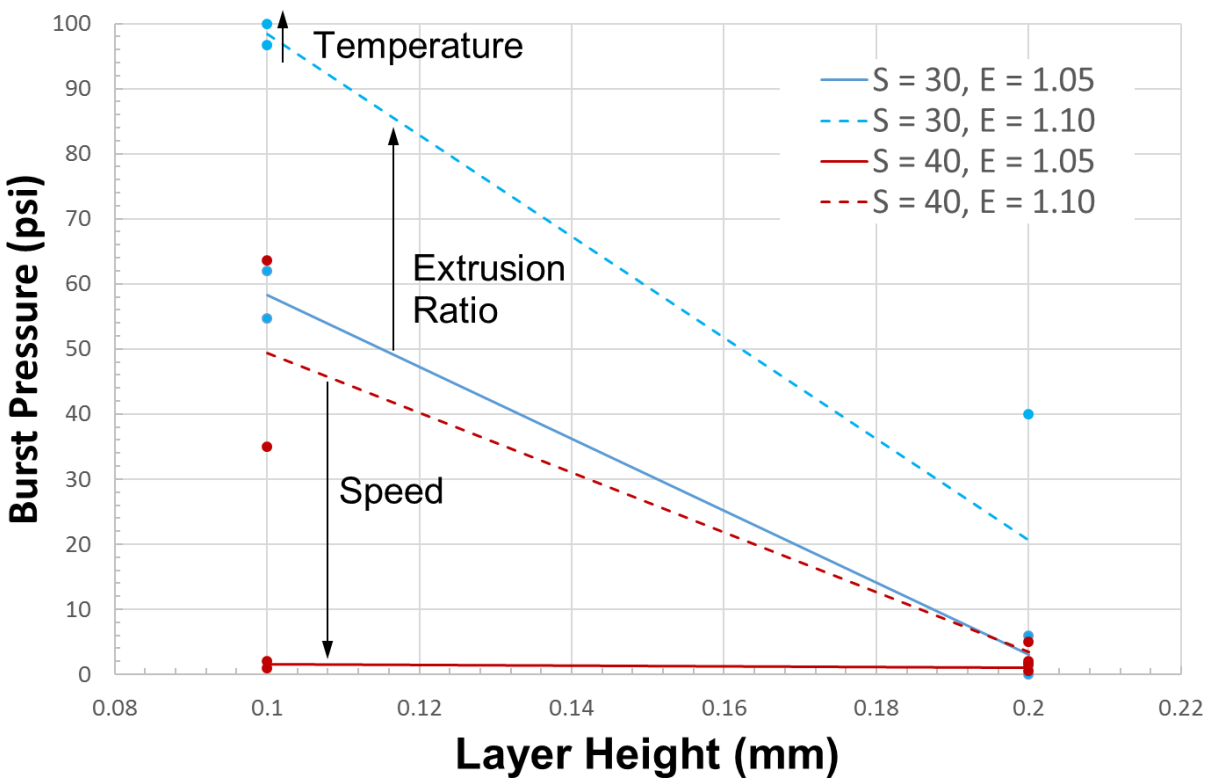

Figure 47: Kazoo Pressurization DoE Setup and Results

7.3.4.2 Failure Modes

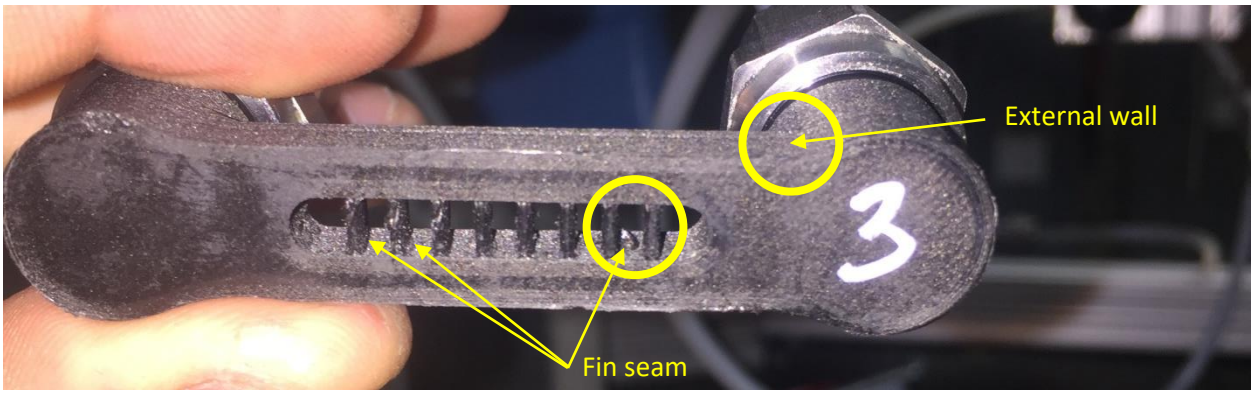

Figure 48: Kazoo pressurization failure modes

7.3.5 Full-Scale Waterside Pressure Drop

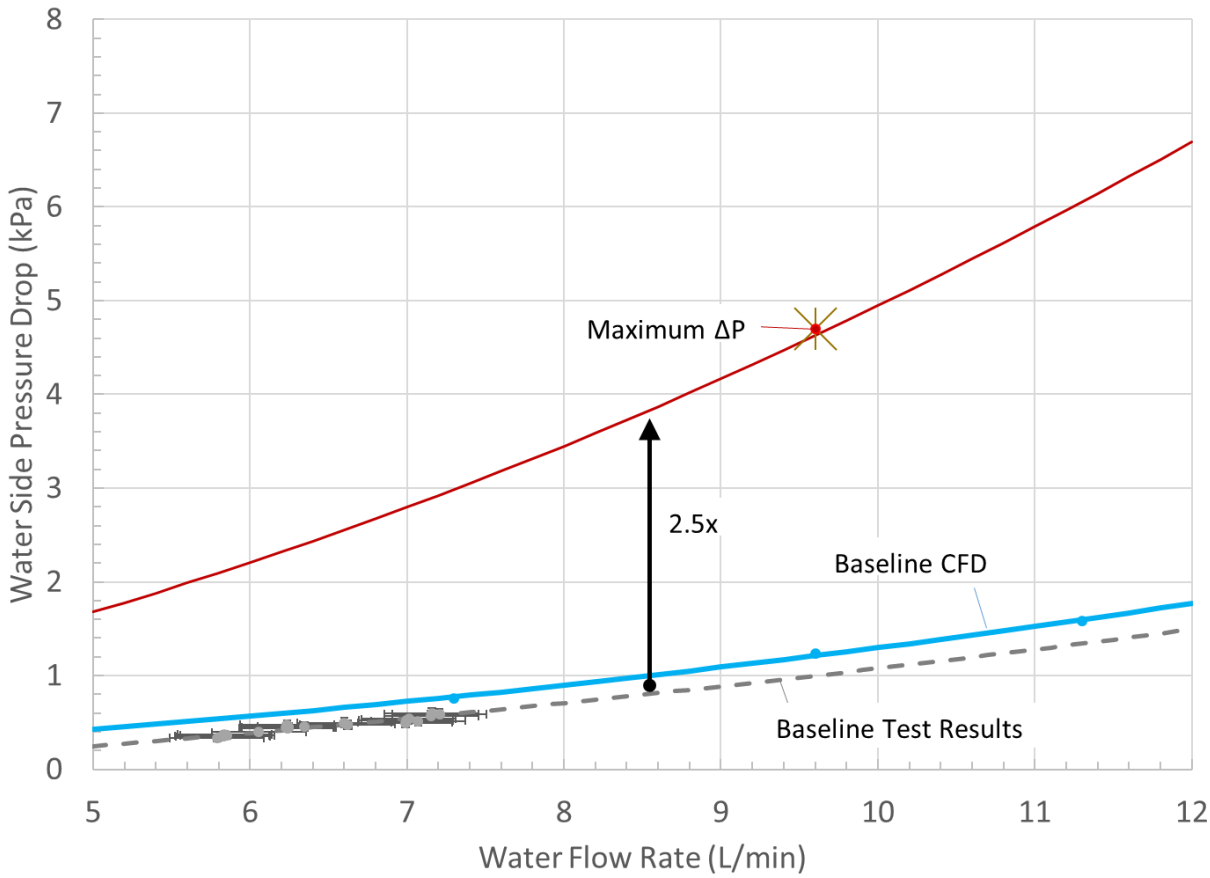

Figure 49: Baseline full-scale waterside modeling and test resutls compared to maximum allowable pressure drop